

JWST Advanced Deep Extragalactic Survey (JADES) Data Release 5: Photometric Catalog

BRANT E. ROBERTSON ,¹ BENJAMIN D. JOHNSON ,² SANDRO TACCHELLA ,^{3,4} DANIEL J. EISENSTEIN ,²
 KEVIN HAINLINE ,⁵ STACEY ALBERTS ,^{5,6} SANTIAGO ARRIBAS ,⁷ WILLIAM M. BAKER ,⁸ ANDREW J. BUNKER ,⁹
 ALEX J. CAMERON ,⁹ STEFANO CARNIANI ,¹⁰ COURTNEY CARREIRA ,¹ JACOPO CHEVALLARD ,⁹
 CHIARA CIRCOSTA ,¹¹ EMMA CURTIS-LAKE ,¹² A. LOLA DANHAIVE ,^{3,4} QIAO DUAN ,^{3,4} EIICHI EGAMI ,⁵
 RYAN HAUSEN ,¹³ JAKOB M. HELTON ,¹⁴ ZHIYUAN JI ,⁵ ROBERTO MAIOLINO ,^{3,4,15} PABLO G. PÉREZ-GONZÁLEZ ,⁷
 DÁVID PUSKÁS ,^{3,4} MARCIA RIEKE ,⁵ PIERLUIGI RINALDI ,¹⁶ FENGWU SUN ,² YANG SUN ,⁵ HANNAH ÜBLER ,¹⁷
 JAMES A. A. TRUSSLER ,² NATALIA C. VILLANUEVA ,¹⁸ LILY WHITLER ,^{3,4} CHRISTINA C. WILLIAMS ,¹⁹
 CHRISTOPHER N. A. WILLMER ,⁵ CHRIS WILLOTT ,²⁰ ZIHAO WU ,² AND YONGDA ZHU ,⁵

THE JADES COLLABORATION

¹ Department of Astronomy and Astrophysics, University of California, Santa Cruz, 1156 High Street, Santa Cruz, CA 95064, USA

² Center for Astrophysics | Harvard & Smithsonian, 60 Garden St., Cambridge MA 02138 USA

³ Kavli Institute for Cosmology, University of Cambridge, Madingley Road, Cambridge, CB3 0HA, UK

⁴ Cavendish Laboratory, University of Cambridge, 19 JJ Thomson Avenue, Cambridge, CB3 0HE, UK

⁵ Steward Observatory, University of Arizona, 933 N. Cherry Avenue, Tucson, AZ 85721, USA

⁶ AURA for the European Space Agency (ESA), Space Telescope Science Institute, 3700 San Martin Dr., Baltimore, MD 21218, USA

⁷ Centro de Astrobiología (CAB), CSIC-INTA, Cra. de Ajalvir Km. 4, 28850- Torrejón de Ardoz, Madrid, Spain

⁸ DARK, Niels Bohr Institute, University of Copenhagen, Jagtvej 155A, DK-2200 Copenhagen, Denmark

⁹ Department of Physics, University of Oxford, Denys Wilkinson Building, Keble Road, Oxford OX1 3RH, UK

¹⁰ Scuola Normale Superiore, Piazza dei Cavalieri 7, I-56126 Pisa, Italy

¹¹ Institut de Radioastronomie Millimétrique (IRAM), 300 Rue de la Piscine, 38400 Saint-Martin-d'Héres, France

¹² Centre for Astrophysics Research, Department of Physics, Astronomy and Mathematics, University of Hertfordshire, Hatfield AL10 9AB, UK

¹³ Department of Physics and Astronomy, The Johns Hopkins University, 3400 N. Charles St., Baltimore, MD 21218

¹⁴ Department of Astronomy & Astrophysics, The Pennsylvania State University, University Park, PA 16802, USA

¹⁵ Department of Physics and Astronomy, University College London, Gower Street, London WC1E 6BT, UK

¹⁶ Space Telescope Science Institute, 3700 San Martin Drive, Baltimore, Maryland 21218, USA

¹⁷ Max-Planck-Institut für extraterrestrische Physik (MPE), Gießenbachstraße 1, 85748 Garching, Germany

¹⁸ Department of Astronomy, The University of Texas at Austin, Austin, TX, USA

¹⁹ NSF National Optical-Infrared Astronomy Research Laboratory, 950 North Cherry Avenue, Tucson, AZ 85719, USA

²⁰ NRC Herzberg, 5071 West Saanich Rd, Victoria, BC V9E 2E7, Canada

ABSTRACT

The JWST Advanced Deep Extragalactic Survey (JADES) provides deep, multi-wavelength imaging and spectroscopy of the GOODS-North and GOODS-South fields, enabling studies of galaxy formation and evolution from the local universe to the first few hundred million years after the Big Bang. We present the public release of the JADES Data Release 5 (DR5) photometric catalogs and describes the methodologies used for source detection, deblending, photometry, uncertainty estimation, and catalog curation. The catalogs are constructed from 35 space-based imaging mosaics obtained with JWST/NIRCam, JWST/MIRI, HST/ACS, and HST/WFC3, combining approximately 1250 hours of JADES imaging with extensive additional public JWST and HST observations in the GOODS fields. Sources are identified using custom signal-to-noise-based detection and deblending algorithms optimized for the depth, resolution, and complex point-spread-function structure of JWST imaging. Source centroids, shapes, and photometric apertures are determined using a new fast two-dimensional Gaussian regression method applied to detection-image profiles. We provide forced circular-aperture photometry, ellipsoidal Kron photometry, and curve-of-growth measurements for every source in every

band. We introduce a new pixel-level regression framework to model photometric uncertainties as a function of aperture size and local mosaic properties, accounting for correlated noise in heterogeneous JWST mosaics. Photometric redshifts are computed using template-based fitting applied to both small-aperture photometry on unconvolved images and Kron photometry on common-PSF mosaics. The JADES DR5 catalogs supersede previous JADES photometric releases, and are publicly released through the Mikulski Archive for Space Telescopes and an interactive web interface.

Keywords: Catalogs (205) — Galaxies (573) — High-redshift galaxies (734) — Surveys (1671) — James Webb Space Telescope (2291)

1. INTRODUCTION

In the span of a few short years, James Webb Space Telescope (JWST) has completely rewritten our view of the distant cosmos. By discovering a host of galaxies at distances beyond what was widely thought probable (e.g., M. Castellano et al. 2022; R. P. Naidu et al. 2022; S. L. Finkelstein et al. 2022; B. E. Robertson et al. 2023; E. Curtis-Lake et al. 2023; K. N. Hainline et al. 2024; B. Robertson et al. 2024; S. Carniani et al. 2024; R. P. Naidu et al. 2025), JWST has expanded the horizon of the universe of tangible things past redshift $z \sim 14$ to the first 300 million years of cosmic time. Such discoveries have already addressed many of the open questions about the epoch of cosmic reionization left unanswered before JWST (for a review, see B. E. Robertson 2022) and posed even more about the efficiency of early galaxy formation, the origins of the first stars, and the beginnings of cosmic reionization.

The data used to search for the most distant galaxies serves many scientific purposes, and the uniform reduction and analysis of extragalactic survey fields provide a foundation for studies of galaxy formation and evolution across cosmic time (e.g., T. Treu et al. 2022; R. A. Windhorst et al. 2023; P. A. Oesch et al. 2023; C. M. Casey et al. 2023; S. L. Finkelstein et al. 2025), including the assembly of stellar mass (A. Weibel et al. 2024; M. Shuntov et al. 2025a), the growth of structure (e.g., A. Weibel et al. 2025), and the emergence of diverse galaxy populations (C. T. Donnan et al. 2024), while simultaneously enabling the discovery of faint sources in the nearby Universe, such as brown dwarfs in the Milky Way (e.g. D. Langeroodi & J. Hjorth 2023; A. J. Burgasser et al. 2024; K. N. Hainline et al. 2025). In this context, several major JWST/NIRCam imaging programs have released deep extragalactic datasets accompanied by public photometric catalogs, including CEERS (I. G. Cox et al. 2025) and COSMOS-Web (M. Shuntov et al. 2025b). Independent analyses have generated source catalogs from public JWST imaging, such as the Astrodeep project (E. Merlin et al. 2024). Together, these efforts span a wide range of survey strategies in depth, area, and filter coverage, and have rapidly transformed studies of galaxy evolution, from the statistical properties of galaxy populations to the identification of rare objects at both high and low redshift.

As part of the JWST Advanced Deep Extragalactic Survey (JADES; M. Rieke 2020; A. J. Bunker et al. 2020; D. J. Eisenstein et al. 2023) Data Release 5 (DR5), this paper presents the detection, deblending, and source characterization methods, as well as catalogs containing forced aperture photometry, photometric redshifts, and curves-of-growth for 35 space-based mosaic images acquired with JWST NIRCam, JWST MIRI, HST ACS, and HST WFC3 over the Great Observatories Origins Deep Survey (GOODS) North and South Fields. The catalogs are constructed from sources detected in the JADES DR5 mosaics detailed in a companion paper (B. D. Johnson et al. submitted, hereafter J26).

We provide an overview of imaging data from J26 used for cataloging in Section 2. Since these images leverage public JWST community surveys in GOODS-N and GOODS-S in addition to the ~ 1250 JWST observation hours of JADES imaging in these fields, we provide detailed references to all the JWST programs used in constructing our catalogs in Section 2. As discussed in J26 and Section 7.5, the JADES DR5 release provides a new methodology for hash encoding the list of JWST programs contributing to the measurements for every source and reports that information in the catalogs. The methods for constructing detection and deblending images, identifying and separating sources, and curating the resulting source catalogs are detailed in Section 3. We present the techniques we employ to model the individual source properties, including a new method for fast two-dimensional Gaussian regression for modeling the source flux profiles, and determine the R. G. Kron (1980) photometry ellipsoidal apertures in Section 4. Section 5 details the model JWST NIRCam and MIRI and empirical HST point spread function construction, followed by a presentation of the methodology for creating common-PSF images in Section 6. The schema for data quality and context flagging for the catalogs is discussed in Section 7. In Section 8, we detail a new regression model for generating mosaics of the photometric uncertainty scaling, using the pipeline variance image as a template for the single-pixel

limit of the sky background. Forced circular aperture and Kron photometry on all sources are detailed in Section 9, and the curve-of-growth measurements for all sources discussed in Section 10. The photometric redshift catalog generation is presented in Section 11. We summarize the main text and provide data access instructions in Section 12. The Appendix A provides detail on the format for all components of the catalog.

2. OVERVIEW OF IMAGING DATA

Table 1 summarizes the filter set, areal coverage, and median depths of the HST/ACS, HST/WFC3, JWST/NIRCam, and JWST/MIRI imaging data. The JADES NIRCam Data Release 5 imaging data are presented by J26, including all the NIRCam filter mosaics that form the core dataset for the detection, deblending, and photometric analysis presented in this work. The NIRCam data are drawn primarily from the JADES JWST Programs 1180, 1181, 1210, 1286, and 1287 (D. J. Eisenstein et al. 2023), and the JADES Origins Field Program 3215 (D. J. Eisenstein et al. 2025). We also include deep NIRCam imaging in the same fields from the Next Generation Deep Extragalactic Exploratory Public (NGDEEP) Survey (M. B. Bagley et al. 2024), (G. Östlin et al. 2025), the MIRI Deep Imaging Survey (MIDIS; P. G. Pérez-González et al. 2024; G. Östlin et al. 2025), the JWST Extragalactic Medium-band Survey (JEMS; C. C. Williams et al. 2023), Prime Extragalactic Areas for Reionization and Lensing Science (PEARLS) Survey (R. A. Windhorst et al. 2023), the Bias-free Extragalactic Analysis for Cosmic Origins with NIRCam survey (T. Morishita et al. 2025), and JWST Program 6511 (P. G. Pérez-González et al. 2025). The mosaics incorporate wider area data from the First Reionization Epoch Spectroscopically Complete Observations (FRESCO) Survey (P. A. Oesch et al. 2023), the Parallel wide-Area Nircam Observations to Reveal And Measure the Invisible Cosmos (PANORAMIC) Survey (C. C. Williams et al. 2025), the Public Observation Pure Parallel Infrared Emission-Line Survey (POPPIES; J. Kartaltepe et al. 2024), and the Slitless Areal Pure-Parallel HIgh-Redshift Emission Survey (SAPPHIRES; F. Sun et al. 2025).

For the MIRI data, the JADES MIRI parallel imaging described by S. Alberts et al. (submitted, hereafter A26) is combined with the Systematic Mid-infrared Instrument Legacy Extragalactic Survey (SMILES; G. H. Rieke et al. 2024) public release mosaics (S. Alberts et al. 2024), following the mosaic stacking methods described in J26. JADES MIRI parallel imaging includes deep F770W imaging in GOODS-S, medium F770W, F1280W, and F1500W parallels in GOODS-S, and F770W and F1280W parallels in GOODS-N. The F560W, F1800W, F2100W, and F2550W imaging used for our catalogs are taken directly from the SMILES release and reprojected to our mosaic pixel footprint before processing.

For the HST data, we use the Hubble Legacy Fields (HLF) mosaics (G. Illingworth et al. 2016; K. E. Whitaker et al. 2019) and include HST/ACS F435W, F606W, F775W, F814W, F850LP and HST/WFC3 F105W, F125W, F140W, and F160W imaging in our analysis. We use the HLF GOODS-S v2.0 and GOODS-N v2.5 mosaics, re-registered to the JWST NIRCam mosaic astrometric frame, reprojected to the JWST mosaic pixel scale, and culled to the same mosaic footprint.

3. DETECTION

The depth and resolution of the JWST imaging provides an opportunity to construct sensitive multi-band stacks to detect faint sources and low-surface brightness exteriors of extended objects, separate complex interacting and overlapping sources, and accurately measure the shapes and sizes of galaxies across cosmic time. At a high-level our approach for object detection and segmentation follows the previous approaches employed in prior JADES data releases and analyses (M. J. Rieke et al. 2023; D. J. Eisenstein et al. 2025; F. D'Eugenio et al. 2025a; Z. Ji et al. 2024; B. Robertson et al. 2024), but some of the details are presented thoroughly here for the first time.

The key features of the detection process include the construction of the detection and deblending images, which are composed of signal-to-noise ratio (SNR) stacks of the mosaics presented by J26, and the detection and deblending algorithms. Separate signal (i.e., flux) and noise stacked images are generated, and then the ratio of the images used to construct an SNR mosaic when appropriate. We present the details of how these signal and noise mosaics are constructed and combined into detection and deblending images below in Sections 3.1-3.3. The custom detection and deblending methods that identify and separate distinct sources are described in Sections 3.4, 3.4.1, and 3.4.2. These methods have been demonstrated previously to provide high-quality detection completeness for faint sources (B. Robertson et al. 2024) and have found success in identifying very distant high-redshift sources that are both compact and isolated (B. E. Robertson et al. 2023) or extended and confused with foreground interlopers (e.g., B. Robertson et al. 2024; K. N. Hainline et al. 2024; S. Carniani et al. 2024). Once the sources have been detected and deblended,

Table 1. Summary of Imaging Data from J26

| Filter | Wavelength [μm] | GOODS-S Area [arcmin 2] | GOODS-S Depth [AB] | GOODS-N Area [arcmin 2] | GOODS-N Depth [AB] |
|-------------------|---------------------------------|--------------------------------|-----------------------|--------------------------------|-----------------------|
| HST/ACS F435W | 0.433 | 272.19 | 28.55 | 222.64 | 28.65 |
| HST/ACS F606W | 0.592 | 481.81 | 28.24 | 233.37 | 28.67 |
| HST/ACS F775W | 0.769 | 284.31 | 28.12 | 241.40 | 28.35 |
| HST/ACS F814W | 0.806 | 390.25 | 27.99 | 295.73 | 28.52 |
| HST/ACS F850LP | 0.904 | 479.14 | 27.08 | 240.16 | 27.77 |
| HST/WFC3 F105W | 1.055 | 118.05 | 27.89 | 153.72 | 27.61 |
| HST/WFC3 F125W | 1.249 | 181.41 | 27.77 | 170.90 | 27.41 |
| HST/WFC3 F140W | 1.392 | 151.56 | 26.40 | 117.46 | 26.66 |
| HST/WFC3 F160W | 1.537 | 221.71 | 27.21 | 170.78 | 27.22 |
| JWST/NIRCam F070W | 0.705 | 72.18 | 29.18 | 30.40 | 28.87 |
| JWST/NIRCam F090W | 0.902 | 159.42 | 29.66 | 125.42 | 29.43 |
| JWST/NIRCam F115W | 1.154 | 210.47 | 29.78 | 180.37 | 28.91 |
| JWST/NIRCam F150W | 1.501 | 213.93 | 29.83 | 139.16 | 29.04 |
| JWST/NIRCam F162M | 1.627 | 33.31 | 29.65 | 14.77 | 28.87 |
| JWST/NIRCam F182M | 1.845 | 87.81 | 29.08 | 109.50 | 28.73 |
| JWST/NIRCam F200W | 1.988 | 233.71 | 29.73 | 174.31 | 29.40 |
| JWST/NIRCam F210M | 2.096 | 76.63 | 28.67 | 78.98 | 28.41 |
| JWST/NIRCam F250M | 2.503 | 36.17 | 29.29 | — | — |
| JWST/NIRCam F277W | 2.777 | 210.44 | 30.07 | 115.01 | 29.61 |
| JWST/NIRCam F300M | 2.996 | 34.50 | 29.85 | 9.07 | 29.07 |
| JWST/NIRCam F335M | 3.362 | 119.45 | 29.71 | 78.62 | 29.12 |
| JWST/NIRCam F356W | 3.565 | 214.16 | 30.07 | 155.14 | 29.38 |
| JWST/NIRCam F410M | 4.084 | 157.52 | 29.42 | 110.79 | 28.85 |
| JWST/NIRCam F430M | 4.281 | 10.07 | 28.71 | 8.74 | 28.20 |
| JWST/NIRCam F444W | 4.402 | 231.18 | 29.60 | 207.53 | 28.84 |
| JWST/NIRCam F460M | 4.630 | 10.08 | 28.28 | 8.77 | 27.78 |
| JWST/NIRCam F480M | 4.817 | 18.07 | 28.65 | — | — |
| JWST/MIRI F560W | 5.645 | 35.30 | 25.65 | — | — |
| JWST/MIRI F770W | 7.639 | 58.34 | 25.77 | 9.46 | 26.50 |
| JWST/MIRI F1000W | 9.953 | 34.57 | 24.51 | — | — |
| JWST/MIRI F1280W | 12.810 | 52.48 | 23.81 | 9.28 | 24.71 |
| JWST/MIRI F1500W | 15.064 | 58.13 | 23.53 | — | — |
| JWST/MIRI F1800W | 17.983 | 36.06 | 22.31 | — | — |
| JWST/MIRI F2100W | 20.795 | 36.02 | 21.76 | — | — |
| JWST/MIRI F2550W | 25.364 | 36.23 | 19.57 | — | — |

NOTE—We report aperture-corrected 5- σ point source depths, computed as the median value of the model uncertainty image for $r = 0.1''$ apertures calculated following the method described in Section 8.1. As discussed in [D. J. Eisenstein et al. \(2025\)](#), for NIRCam these depths agree well with expectations from the JWST Exposure Time Calculator ([K. M. Pontoppidan et al. 2016](#)).

the catalogs are curated as described in Section 3.5, source structural properties measured (Section 4.2), and then photometry performed (Section 9).

Figure 1 illustrates the process of detection and source characterization detailed in this Section. The upper left panel shows an RGB composite of the multi-band imaging for a portion of the JADES Origins Field ([D. J. Eisenstein et al.](#)

2025) in GOODS-S from J26, including the source JADES-GS-z14-0 (S. Carniani et al. 2024). The long-wavelength NIRCam filters are stacked to create the detection image (a logarithmic projection is shown in the upper right panel of Figure 1) and the short-wavelength NIRCam filters near $\lambda \approx 2\mu\text{m}$ are used during deblending. The result of the detection and deblending algorithm produces a segmentation map, as shown in the lower left panel. The Gaussian regression modeling of the source properties then (see Section 4 below) allow for the estimation of Kron photometry apertures, as shown as overlays on a harsh stretch of the detection image in the lower right panel of Figure 1. We now turn to describing the detection image construction, and the detection and deblending methods.

3.1. Noise Images

To construct a weighted SNR image for the JWST NIRCam images, the signal and noise image for every filter must be defined. The noise image can be directly estimated from the `ERR` HDU image extension supplied by the `jwst` pipeline mosaics constructed as described by J26. However, since the noise image appears in the denominator, unexpected pixel-level variations in the noise can lead to artificial spikes in the significance level of detected objects. For various versions of the `jwst` pipeline this indeed occurred, with occasional small but non-zero pixels present in the `ERR` images leading to spikes in the resulting SNR images used for detection. To avoid such possible issues, we construct a separate “noise mosaic” from the `ERR` mosaics. For each filter, the `ERR` mosaic is squared to form a variance mosaic that is median filtered with a 5×5 boxcar window. The square root of the filtered variance mosaic is then computed to obtain a filtered noise mosaic. Finally, the ratio of the original `ERR` mosaic and the filtered noise mosaic is calculated, and any non-zero pixel in the original `ERR` mosaic with a ratio < 0.9 is replaced by the corresponding pixel in the filtered noise mosaic. This procedure successfully eliminated the `ERR` mosaic divots occasionally present in the images processed using the `jwst` pipeline and prevented the corresponding SNR spikes that could lead to spurious detections.

3.2. Detection Image

For our detection images, we compute inverse-variance-weighted signal-to-noise ratio mosaics by combining the individual mosaics from JWST long-wavelength filters. The variance images used in weighting are determined by squaring the noise mosaics constructed as described in Section 3.1. The combined signal mosaic is constructed by summing the `SCI` mosaic for each filter, inversely weighted by its variance image, and then dividing by the sum of the inverse variance images. The combined noise mosaic is computed by taking the inverse square root of the sum of the inverse variance images. The SNR image used for detection is the ratio of these combined signal and noise mosaics. We note that we use the mosaics without PSF-matching to construct the SNR images. Using common-PSF images could reduce chromaticity in the detection image at the expense of reduced signal-to-noise in low surface brightness regions around galaxies.

The GOODS-N and GOODS-S fields have differing filter coverage. In GOODS-N, we combine F277W, F335M, F356W, F410M, F430M, F444W, and F460M where available in constructing the detection image. In GOODS-S, we additionally include F480M where available.

In GOODS-N, in the region of the field covered with LW data only from the POPPIES program (PID 5398), the F444W imaging is shallow. For improved signal-to-noise, we therefore add the F200W subregion mosaics from the `jw053980.gn_pa220`, `jw053980.gn_pa227`, and `jw053980.gn_pa230` regions to the detection image. See J26 for a description of the subregion mosaics.

The JADES imaging includes MIRI parallel observations in GOODS-N and MIRI parallels in GOODS-S that are stacked with the SMILES MIRI mosaics, leading to regions of the fields where there is MIRI imaging without NIRCam coverage. For these regions, we include MIRI-generated SNR image subregions constructed from the `SCI` and `ERR` HDUs of the MIRI mosaics processed with the `jwst` pipeline.

Lastly, the ordering and placement of the JADES NIRSpec observations required some targeting to be performed based on HST-only regions of the field that do not have JWST coverage. To support these NIRSpec observations, we generate SNR detection images based on the HLF HST mosaics. For the signal mosaic, we combine the flux HDUs from the HST ACS F775W, F814W, and F850LP filter mosaics using inverse-variance weighting. The noise images used in the SNR image and for weighting are computed following the uncertainty mosaic method described in Section 8.1 below, computing the random aperture uncertainties in circular apertures of radius $r = 0.25''$. We limit the regions where HST-based SNR detection image contributions are added to areas where JADES NIRSpec spectroscopic targeting from HST-detected sources was used.

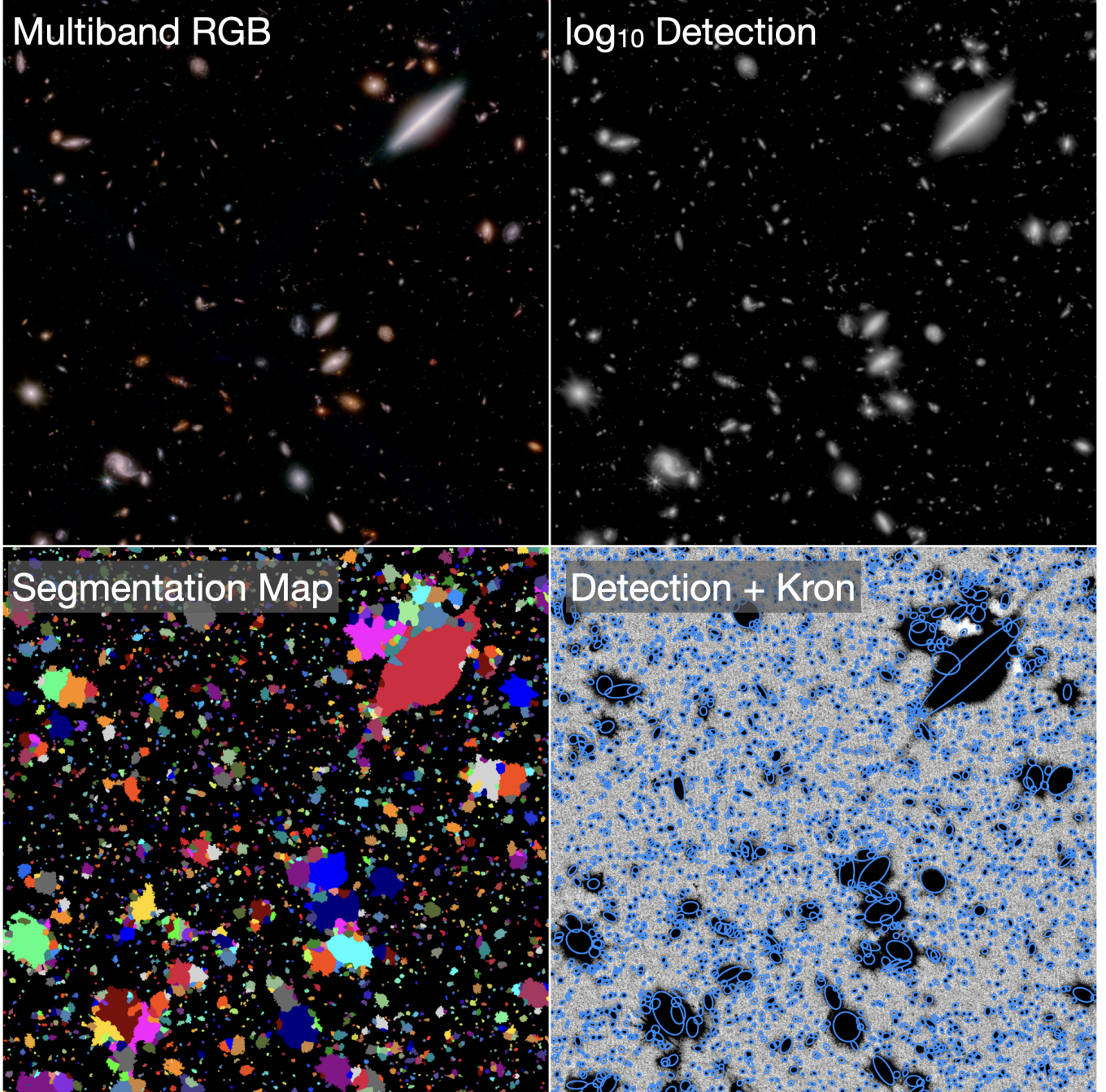


Figure 1. Overview of the detection and deblending process. The multi-band NIRCam imaging from J26 forms the core data used to detect and isolate sources, shown as an RGB composite of the JADES Origins Field region (D. J. Eisenstein et al. 2025) of GOODS-S (upper left). The long-wavelength NIRCam images are stacked to form a deep multi-band detection image that provides the pixel-level signal-to-noise ratio of sources (upper right; logarithmic projection), while a multi-band stack of short-wavelength NIRCam filters near $\lambda \sim 2\mu\text{m}$ are used to deblend sources. Using the detection and deblending methods described in Section 3, a segmentation map of pixel assignments to individual sources is created (lower left). The properties of these pixels are used in a new Gaussian regression model to determine source sizes and R. G. Kron (1980) photometry apertures for each source, shown as ellipsoidal overlays on a harsh stretch of the detection image in the lower right panel and described in Section 4.

The final SNR detection image used in the detection algorithm is then the composite of these separate SNR images, using only the JWST NIRCam SNR image in any area where the NIRCam, MIRI, or HST SNR detection submosaics overlap.

3.3. Deblending Image

While the detection image is constructed from the long wavelength mosaic data, there are higher resolution NIRCam data available at shorter wavelengths over most of the GOODS-S and GOODS-N fields with sufficient depth to support a deblending image to match the detection image. Given the expected redshift distribution and reddening of known sources, we expect that the majority of sources detected in the bluest long wavelength NIRCam filters will also be detected in the reddest short wavelength NIRCam filters at wavelengths $\lambda \approx 2\mu\text{m}$. We therefore construct a deblending image as an inverse-variance-weighted SNR image combining the F182M, F200W, and F210M in each field. Where these short wavelength NIRCam filters are unavailable, we substitute the NIRCam detection SNR image, the HST SNR detection image, and then MIRI detection image, in that order of preference, ensuring that all regions of the detection image are covered by valid pixels in the composite deblending image. In what follows, we will use the symbol SNR_D when referring to the SNR of a pixel or source in the deblending image.

3.4. Detection and Deblending Algorithms

The source catalog generated from the JADES DR5 imaging uses a segmentation map-based approach where a series of detection criteria are applied to pixels in a detection image to define regions containing sources, deblending criteria are applied to detected regions to define separate sources within contiguous detected regions, and then an integer segmentation map labeling pixels with unique source IDs defines the pixels belonging to each object. The segmentation maps are used with customized versions of the `photutils` routine `SourceCatalog` to generate object catalogs, as described in Section 4. The rest of this Section describes how the segmentation maps that feed into the source catalog procedure are generated, including the detection and deblending methods.

3.4.1. Initial Blended Segmentation

A first blended segmentation is created using the `photutils` routine `detect_sources` applied to the maximum of the detection and deblending SNR images smoothed with a gaussian with a half-pixel standard deviation, using a threshold of $SNR > 1.5$ over a minimum of 1 pixel regions. The resulting segments are refined then using a series of morphological processing algorithms. We apply the `scipy.ndimage` routine `binary_fill_holes` to fill any gaps in the segments and relabel the segments using `scipy.ndimage.label`. The segment exteriors are reshaped by the following sequence: 1) dilation using `scipy.ndimage.expand_labels`, 2) eroded twice using a four-connected kernel with `scipy.ndimage.binary_erosion`, 3) dilated once, 4) opened twice using an eight-connected kernel with `scipy.ndimage.binary_opening`, 4) dilated once, 5) holes filled, and then 6) relabeled. This series of operations helps to refine the boundaries of the source segments, but small sources can be eliminated by the erosion and opening operations. Using the resulting segmentation map as a mask, a `detect_sources` pass with $SNR > 3.5$ over a minimum of 4 0.03" pixel regions is performed, any additional recovered sources are dilated once using `expand_labels`, and the segmentation maps merged.

Some additional processing of the initial segmentation map is performed before detailed deblending. An initial source catalog from the segmentation map and detection image is generated. Looping over the objects, thin tenuous connections between distinct objects are broken by eroding each object's segmentation with four iterations. If this erosion splits segments into multiple objects, the objects are relabeled and `expand_labels` is used to regrow their segments to fill the original extent of their parent's footprint.

Once the tenuous connections are broken, the source catalog is again rebuilt. The sources are each investigated to remove any segmentation map fragments that would have failed the original detection conditions. Approximately, this means fragments that do not have a median $SNR > 3$ in either the detection or deblending image. Such sources are removed, as are objects with areas below six pixels. The sources in the resulting segmentation map are then considered for possible deblending.

3.4.2. Deblending

Once the initial blended segmentation map has been generated, a catalog is created and each source inspected. The region of the deblending image delineated by the bounding box of each object's segment is extracted, a floor

of $SNR_D = 1.5$ applied, and then `detect_sources` used to find any sources in the deblending image within the segmentation with $SNR_D > 1.5$ and larger than four pixels. Holes in the segmentation map of these deblended objects are filled and a single `binary_opening` pass with an eight-connected kernel applied. Any sources with $SNR_D > 3.5$ and areas larger than four pixels removed by the opening algorithm are added back to the segmentation map, and two dilation iterations using `expand_labels` are applied. If no additional sources are found by the deblending algorithm within the segmentation derived from the detection image, then the object is not deblended and its original segment is retained. Otherwise, the object is marked for deblending.

If the object is marked for deblending, the deblending algorithm identifies locally dominant peaks in the deblending images and iteratively assigns pixels within the object segment to the deblended peaks following a set of conditions. Local maxima in the deblending image are determined using the `scipy.ndimage.maximum_filter` routine with a disk filter of radius $r = 3$ pixels. These SNR peaks in the deblending image are then candidate locations for newly deblended objects, but the algorithm only retains the peaks that dominate their locale in the deblending image. For the purposes of the algorithm, we define local dominance for a peak as having the largest maximum among peaks in a region defined by a minimum SNR that is some multiplicative fraction ξ of the peak maximum p_{SNR} . In other words, a peak with maximum SNR p_{SNR} is locally dominant if it is the highest peak within an iso-significance contour ξp_{SNR} that surrounds it. For this catalog, we take $\xi = 0.5$.

Procedurally, the algorithm considers the list of peaks sorted by descending SNR. Starting with the highest peak with SNR $p_{SNR,0}$, any candidate peaks within an iso-significance contour $\xi p_{SNR,0}$ are discarded from further consideration as they are locally subdominant. If there are no remaining candidate peaks, there is only one dominant peak, all the remaining pixels are assigned to the singular peak such that the original and deblended segmentations for the region match, and the algorithm moves on to deblending the next object from the initial blended segmentation map. Otherwise, the next highest peak with SNR $p_{SNR,1}$ in the list of candidate subregions is considered. First, all pixels within a contour $p_{SNR,1}$ about the first peak can be safely assigned to it. Then, all lower-SNR peaks within an iso-significance contour $\xi p_{SNR,1}$ about the second peak are removed from consideration.

Once more than one peak has been deblended, decisions about how to assign pixels to distinct peaks must be made. Choices in the literature range from the flux contrast peak assignment method from [Source Extractor \(E. Bertin & S. Arnouts 1996\)](#), shared assignment between peaks using forward modeling of source surface brightness profiles as in [SCARLET \(P. Melchior et al. 2018\)](#), and AI/machine learning-based partial attribution models ([R. Hausen & B. Robertson 2022](#)). Here, we use a deterministic approach where we iteratively consider the pixels sorted in descending SNR. Starting with pixels with an SNR equal to the most recently considered peak SNR $p_{SNR,i}$, which are the lowest SNR pixels yet unassigned, they inherit the peak assignment of their highest SNR neighbor, or become the start of the current peak if they are at its local maximum. These pixel assignments continue until $SNR = p_{SNR,i+1}$ of the next lowest peak under consideration is reached. Once the deblending pixel value $SNR = p_{SNR,i+1}$ of the next lowest peak is reached, its local $\xi p_{SNR,i+1}$ iso-significance contour is cleared of lower-significance peaks, and the process of pixel assignments continues until all peaks have been considered.

At this stage in the algorithm, all the locally dominant peaks in the filtered deblending image within the parent segmentations have been identified and pixels greater than a fraction of ξ of their peak SNR assigned to them, accounting for the local proximity of pixels to multiple peaks. Before the remaining pixels are assigned to peaks, we take two additional steps to recover possible objects of interest that may otherwise be lost. First, faint satellites in the exteriors of bright galaxies may fail the locally dominant peak criterion but may be visually distinguishable. To recover these objects, we apply a Scharr filter to the deblending image to attempt a rotationally-invariant edge detection. Within the parent segmentation, we apply `detect_sources` with a threshold of 10 to the Scharr-filtered deblending SNR image over a minimum area of four pixels. The segments from any resulting detections are dilated using `expand_labels` and added to the list of peaks. Second, since the deblending image is bluer than the detection image there are rare sources where the contrast in significance between the $\lambda \approx 2\mu\text{m}$ deblending image and the $\lambda \gtrsim 2.7\mu\text{m}$ detection image leads to missed or poorly deblended extremely red sources in crowded regions. To recover these regions, we look for peaks in the detection image that have an $SNR > 30$ and exceed the deblending SNR by a factor of $10\times$ over an area of at least 10 pixels. Of these regions, we remove those with high eccentricity which are diffraction spikes with chromatic shifts in local SNR maxima. Any remaining red regions are morphologically opened, dilated, filled, and expanded by three pixels, and then merged to augment the existing deblended segmentations.

Once the final collection of deblended peaks within the initial blended detection segmentations have been determined, grown to occupy the local region of the deblending image they dominate, and augmented with edge-detected

sources and highly-reddened sources, the deblended segmentations have to be grown to fill the detection segmentations. A continuation of the algorithm used to assign pixels to peaks during the initial deblending would not fill the segmentation, since pixels in locally subdominant peaks would be left unassigned. Instead, we use a modified version of the `expand_labels` routine that only expands segments into regions that satisfy a user-specified condition. We set this condition to be a SNR threshold, and then iteratively lower the threshold while expanding the deblended peak segments to fill their parent blended segmentations while following iso-significance contours of the deblending image.

One additional heuristic choice is made regarding the growth of deblended segmentations, which was primarily necessitated by the impact of long, high SNR diffraction spikes from stars on the growth of deblended segmentations. With narrow, large-angle extensions of sources intersecting other bright sources in the detection image, we should expect that deblended segmentation maps should be discontinuous and that locally dominant sources should not necessarily end their spatial extent when they encounter another peak that spans narrow regions of the parent segmentation. Accordingly, when a secondary deblended peak encounters the edge of a parent segmentation during the growth phase, it is allowed to grow by another 20 pixels into the parent segmentation. At that point its growth is halted and the dominant peak segmentation is allowed to grow around or past it. The deblended segmentations are cleaned to remove any possible low SNR fragments or segments with areas less than five pixels, and then the deblended segments are grown within the initial blended parent segments to fill any remaining unassigned pixels. This final fill completes the deblending process.

3.4.3. Second-Pass for Isolated Sources

Once the initial segmentation map has been generated, a second simplified detection is performed to improve recovery of faint, compact objects in isolated regions of the imaging. The segmentation map and the mosaic of the subregion mask are dilated by 10 pixels and used to mask the SNR detection image. A second pass of detection in unmasked regions is performed using the `photutils` routine `detect_sources` with a $SNR > 3$ threshold over a minimum of 5 pixel regions. The resulting segmentation map is dilated using two iterations and a disk footprint of radius 2 pixels, holes are filled, and two iterations of binary opening performed. The resulting second-pass segmentation map is then added to the original deblended segmentation map. This combined segmentation map forms the segmentation map that defines the detection source catalog used as input to the catalog curation stage that defines our final source catalog, described in Section 3.5 below.

3.5. Catalog Curation

While the implemented algorithms for detection and deblending find considerable success in identifying faint objects and disentangling complex, crowded regions populated with extended sources, the methods do experience failures. Notably, the deblending algorithm can shred diffraction spikes and the exteriors of extended but high SNR objects. These failure modes can be addressed directly by re-merging the fragmented segments of shredded objects back into their parent segmentation. However, the scale of the images and catalog volume required a method for performing this catalog curation quickly and efficiently. Figure 2 illustrates our solution to this issue. For convenient viewing of the JADES DR5 mosaic data, overlays of our catalog data onto images, and inspection of NIRSpec slit placements, we use an interactive FitsMap ([R. Hausen & B. E. Robertson 2022](#)) website. We have extended the FitsMap interface to create a selection tool that highlights all objects interior to a user-defined polygon and record their source IDs. These IDs could then be submitted via an online form to a cloud-hosted spreadsheet and updated by volunteers from the collaboration who marked collections of objects for re-merging or, occasionally, deletion. The spreadsheet could be automatically downloaded and parsed such that the segmentation map defining sources in the catalogs could be updated to reflect the input user curation. The catalog curation process was performed for both GOODS-S and GOODS-N, and involved less than a percent of all originally detected objects by number.

Figure 2 illustrates the catalog curation process. Using an overlay of detected sources on the FitsMap, objects that are clearly spurious fragmentations, such as shredded diffraction spikes extending from the JWST PSF of bright stars can be identified (far left panel). The interactive selection tool in FitsMap allows for these objects to be bounded by a polygon and isolated from other sources (center left panel). Once selected, the properties of these sources can then be recorded and their properties curated (e.g., merged or deleted) appropriately (center right panel). In the example shown, the shredded diffraction spikes are re-merged into the central star (far right panel).

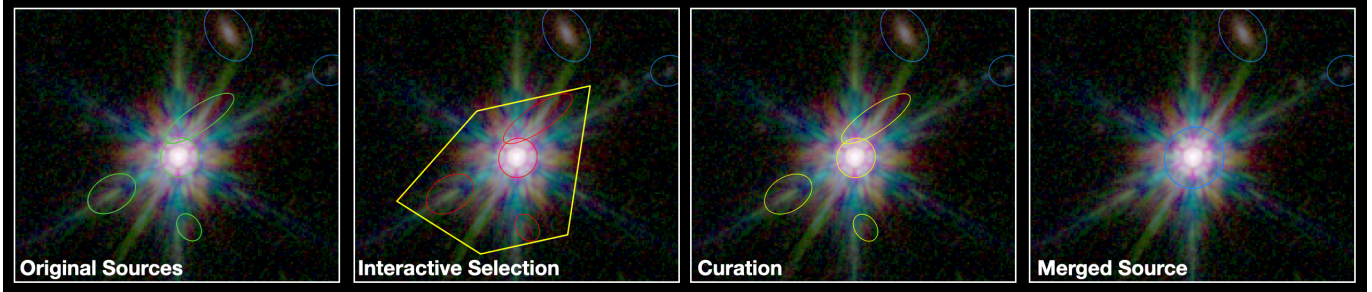


Figure 2. Illustration of the interactive catalog curation tool in FitsMap (R. Hausen & B. E. Robertson 2022) applied to amend the JADES DR5 photometric catalog. Using the source catalog overlay (green ellipses) on the JWST mosaic (RGB), clearly spurious sources in need of curation, such as shredded diffraction spikes, can be identified visually (far left panel). Using the interactive selection tool in FitsMap (left center panel), sources within a polygonal bounding box (yellow line) can be selected (red ellipses) for further processing. Once selected, the object properties can be recorded and the sources marked (yellow ellipses in center right panel) for curation (e.g., merging or deletion). In this case, the diffraction spike shreds are re-merged into the central star (blue ellipse in far right panel).

4. SOURCE CATALOG

Once the deblended segmentation maps have been computed following the methods described in Section 3.4, the source properties required for forced photometry are computed and cataloged. Iterating through each source segmentation, the cataloging method computes a source centroid (Section 4.1) about a local maximum in the detection image.

4.1. *Centroiding*

The centroids for objects are determined from the regions near their peaks, corresponding approximately to the areas in the detection image where the peaks are locally dominant. Within each deblended subregion, the dominant peak in the detection image is located. We restrict the dominant peak not to be adjacent to the edge of the deblended segment to avoid fitting centroids of satellites to peaks in the surrounding background from their host central galaxies. In the vicinity of a peak with detection SNR p_{SNR} , the pixels within iso-significance contour higher than a fraction $\xi = 0.5$ of p_{SNR} are used to compute a SNR-weighted barycenter, which is adopted as the centroid. For objects smaller than 25 pixels, the entire object is instead used to compute a barycenter for the centroid. For reference, we also compute and record barycenters for the entire deblended pixel segmentation from the detection image SNR distribution.

4.2. *Source Properties*

With the centroids computed, the source properties can then be determined from pixels around the centroid locations. We adopt similar methods to those used by the `SourceCatalog` routines implemented by `photutils`. Since we have computed customized centroids, for convenience we re-implement the `SourceCatalog` routines for computing source properties relative to these chosen locations. The central moments are calculated from the object centroid, the object segmentation, and the corresponding detection signal image data. The covariance of the detection signal pixels is then computed from their central moments, following the `SourceCatalog` routine `_covariance`.

Following the `SourceCatalog` methods, we continue by computing and storing the approximate second moments of the detection signal pixel distribution. The semimajor axis size A_p and semiminor axis size B_p are computed from the eigenvalues of the covariance matrix. The eccentricity is computed as $\epsilon_p = \sqrt{1 - B_p^2/A_p^2}$. Here, we denote quantities computed approximating the `photutils` methods with a p subscript. The circularized pixel radius about the centroids are computed from A_p , B_p , and the on-sky orientation θ_p angle computed from the covariance matrix. A R. G. Kron (1980) aperture radius is computed from the first moment of the detection signal pixels within an aperture with a circularized radius six times the second moment, and following `SourceCatalog` the unscaled Kron radius `kron_radius_p` calculated as the ratio of the detection signal-weighted normalized first moment and the sum of the detection signal within the aperture. A minimum unscaled Kron radius is enforced as $\min(\text{kron_radius_p}) = 1.4$, adopting the `photutils` default value.

4.2.1. Gaussian Regression Model for Source Property Estimation

In computing the approximate second moments of the detection signal distribution for each object, the extent of the segmentation used in selecting which pixels contribute to the integrals can influence the resulting object sizes. While we retain and record the object sizes and unscaled Kron radii computed approximating the `photutils` methods, we perform two-dimensional Gaussian regression fits to the detection image profiles of each object to determine directly the Gaussian second moments, orientation on the sky, and the corresponding aperture for determining the Kron radius.

Once the object centroid has been determined, a two-dimensional Gaussian model for an object can be defined as a function of the x and y pixel coordinates relative to the centroid as

$$z(x, y) = K \exp[-(ax^2 + 2bxy + cy^2)]. \quad (1)$$

The amplitude K sets the normalization of the model, and the parameters a , b , and c set the shape of the multivariate elliptical isophotes. The parameters a , b , and c can be related to the Gaussian variances A^2 and B^2 and position angle θ through the formulae

$$A^2 = \frac{1}{2(a \cos^2 \theta + 2b \cos \theta \sin \theta + c \sin^2 \theta)}, \quad (2)$$

$$B^2 = \frac{1}{2(a \sin^2 \theta - 2b \cos \theta \sin \theta + c \cos^2 \theta)}, \quad (3)$$

and

$$\theta = \frac{1}{2} \arctan \left(\frac{2b}{a - c} \right). \quad (4)$$

For convenience, we can re-write Equation 1 as

$$z(x, y) = \exp[\alpha x^2 + 2\beta xy + \gamma y^2 + \delta] \quad (5)$$

with the substitutions $\alpha = -a$, $\beta = -b$, $\gamma = -c$ and $\delta = \log K$. The model represented by Equation 5 can then be fit using an iterative regression scheme to the detection image profile of each object. Here, we extend the one-dimensional weighted Gaussian regression method presented by [H. Guo \(2011\)](#) to multidimensional Gaussian distributions. We can define a metric we wish to optimize when fitting the Gaussian to the detection image profile as

$$\chi^2_W = \sum_i [z_i \log z_i - z_i(\alpha x_i^2 + 2\beta x_i y_i + \gamma y_i^2 + \delta)]^2. \quad (6)$$

Here, the sum over index i runs over the pixels in the object segmentation, x_i and y_i are pixel coordinates relative to the object centroid, and z_i is the value of the i -th pixel. Taking the partial derivatives of this metric with respect to the parameters and setting them equal to zero results in a system of linear equations

$$\begin{bmatrix} \sum z^2 x^4 & 2 \sum z^2 x^3 y & \sum z^2 x^2 y^2 & \sum z^2 x^2 \\ \sum z^2 x^3 y & 2 \sum z^2 x^2 y^2 & \sum z^2 x y^3 & \sum z^2 x y \\ \sum z^2 x^2 y^2 & 2 \sum z^2 x y^3 & \sum z^2 y^4 & \sum z^2 y^2 \\ \sum z^2 x^2 & 2 \sum z^2 x y & \sum z^2 y^2 & \sum z^2 \end{bmatrix} \begin{bmatrix} \alpha \\ \beta \\ \gamma \\ \delta \end{bmatrix} = \begin{bmatrix} \sum z^2 x^2 \log z \\ \sum z^2 x y \log z \\ \sum z^2 y^2 \log z \\ \sum z^2 \log z \end{bmatrix} \quad (7)$$

where we have suppressed the index i , but the sums run over the pixels in the object segmentations. In the presence of noise in the z_i , [H. Guo \(2011\)](#) introduced an iterative scheme for performing a weighted one-dimensional Gaussian regression. We can write an iterative scheme for performing the equivalent two-dimensional Gaussian regression as

$$\begin{bmatrix} \sum z_{(k-1)}^2 x^4 & 2 \sum z_{(k-1)}^2 x^3 y & \sum z_{(k-1)}^2 x^2 y^2 & \sum z_{(k-1)}^2 x^2 \\ \sum z_{(k-1)}^2 x^3 y & 2 \sum z_{(k-1)}^2 x^2 y^2 & \sum z_{(k-1)}^2 x y^3 & \sum z_{(k-1)}^2 x y \\ \sum z_{(k-1)}^2 x^2 y^2 & 2 \sum z_{(k-1)}^2 x y^3 & \sum z_{(k-1)}^2 y^4 & \sum z_{(k-1)}^2 y^2 \\ \sum z_{(k-1)}^2 x^2 & 2 \sum z_{(k-1)}^2 x y & \sum z_{(k-1)}^2 y^2 & \sum z_{(k-1)}^2 \end{bmatrix} \begin{bmatrix} \alpha_k \\ \beta_k \\ \gamma_k \\ \delta_k \end{bmatrix} = \begin{bmatrix} \sum z_{(k-1)}^2 x^2 \log z \\ \sum z_{(k-1)}^2 x y \log z \\ \sum z_{(k-1)}^2 y^2 \log z \\ \sum z_{(k-1)}^2 \log z \end{bmatrix}. \quad (8)$$

As before, the summations run over the pixels in the segmentation. The quantity $\log z$ is computed from the detection image pixel values z_i . The iterated quantities $z_{(k)}$ are computed as

$$z_{(k)} = \begin{cases} z & \text{for } k = 0 \\ e^{\alpha_k x^2 + 2\beta_k x y + \gamma_k y^2 + \delta_k} & \text{for } k > 0 \end{cases} \quad (9)$$

In each iteration, the vector on the right hand side of Equation 8 is multiplied by inverse of the matrix on the left hand side to compute the vector of parameter values. The values $z_{(k)}$ are updated at each iteration with improved solutions for the parameters α_k , β_k , γ_k , and δ_k . The parameter values converge quickly, to within floating-point precision before the maximum number of ten iterations that we enforce on the algorithm.

Figure 3 shows an example of the Gaussian regression method applied to an object in GOODS-S (ID=615). The leftmost panel of the figure shows the distribution of pixel SNR values as a function of the circularized pixel radius from the object centroid, along with the circularized model of the two-dimensional Gaussian over plotted. The middle left panel shows the SNR detection image of pixels in the segmentation assigned to the object, with the $1 - \sigma$ ellipse defined by the semimajor axis A , semiminor axis B , and position angle θ for the object. The middle right panel shows the Gaussian model determined via regression, with the same ellipse overlaid along with annotations indicating the best-fit values of A and B , and the rightmost panel shows the residual between the SNR image and model. As Figure 3 illustrates, the Gaussian regression method we employ both provides an estimate of the source sizes that can be used for further constraints on photometric apertures but also provides an actual model for the source SNR profile that can be compared with the detection image and assessed directly for accuracy via its residuals.

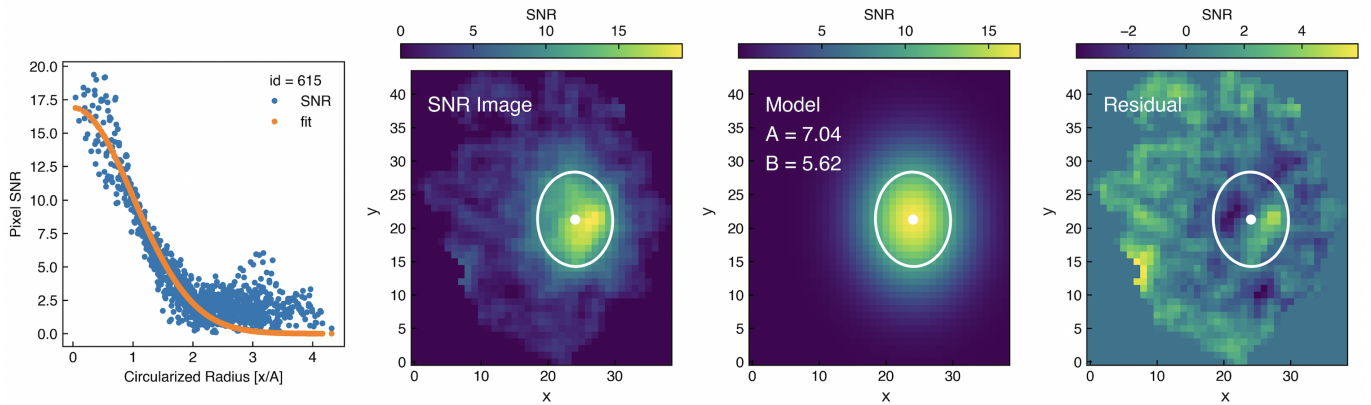


Figure 3. Example of Gaussian regression modeling, shown for object ID=615 from the JADES DR5 GOODS-S region. The pixel SNR data from the detection image (center left panel), masked by the object segmentation. The regression method described in Section 4.2.1 is used to fit a two-dimensional Gaussian profile to the source, as shown in the center right panel. The semimajor and semiminor axes of the best-fit are indicated in pixels, and the 1σ isodensity contour shown as an overlaid white ellipse in the center left, center right, and far right panels. The goodness of fit can be judged from the residual of the SNR image less the model, as shown in the far right panel, and by over plotting the circularized SNR pixel data (blue points) and model (orange curve) as shown in the far left panel.

Once the semimajor axis A (Equation 2), semiminor axis B (Equation 3), and position angle θ (Equation 4) are determined, the `photutils` procedures for computing the Kron apertures are replicated. Pixels within a circularized radius of six times the Gaussian second moments are used to compute the unscaled Kron radius, with a minimum value of 1.4, and the resulting aperture is used in Kron photometry (see Section 9.2 below).

5. POINT SPREAD FUNCTIONS

The process of computing aperture corrections for photometric measurements and generating common-PSF images requires point spread functions for each image. Here we describe our methods for constructing the PSFs we use for our HST, JWST NIRCam, and JWST MIRI photometric analysis.

5.1. Apodization

The two-dimensional PSFs are used for both constructing common-PSF images and for photometric aperture corrections. The methods for constructing empirical and model PSFs that we use generate rectangular image footprints for the PSFs. We note that for each PSF, we apply a circular apodization to ensure that the PSF normalization is computed within a projected radius, rather than within a integrated rectangular area, and to ameliorate possible side lobe artifacts during convolutions caused by effective square wave truncations of the PSF. The multiplicative

apodization we apply is a circular Tukey filter that can be written as

$$T(r, \alpha, \lambda) = \begin{cases} 1 & r < (1 - \alpha)\lambda \\ \frac{1}{2} [1 - \cos(\frac{\pi r}{\alpha\lambda} - \frac{\pi}{\alpha})] & (1 - \alpha)\lambda \leq r < \lambda \\ 0 & r \geq \lambda \end{cases} \quad (10)$$

where r is the fractional radius of a pixel from the center of the PSF in terms of the half-width of the square PSF image, and we choose $\alpha = 0.1$ and $\lambda = 0.995$. The PSFs are renormalized after apodization. Other choices could be made to further reduce the power in side lobes, but we chose the Tukey filter as a compromise to preserve the strength of the prominent JWST diffraction spikes.

5.2. *HST Effective Point Spread Functions*

The HST effective point spread functions (ePSF) used to compute aperture corrections and common-PSF image convolutional kernels are determined from the HLF ACS and WFC3 mosaics using methods from the `photutils` package. Lists of known stars in GOODS-N and GOODS-S are used as input to create separate ePSFs in each HST filter for each field, limiting to stars $18 < m_{AB} < 21$ for ACS filters and $18 < m_{AB} < 22$ for WFC3 filters. Briefly the stars are extracted from the HLF mosaics using the `extract_stars` routine. An `EPSFBuilder` instance is initialized with no oversampling and a maximum of ten iterations, and then applied to the star locations to generate an ePSF, which is then circularly apodized as described in Section 5.1 above. The resulting ePSFs for each filter are visually inspected for artifacts.

5.3. *NIRCam Model Point Spread Functions*

As described in J26 and following methods developed from those presented in [Z. Ji et al. \(2024\)](#), we generate model point spread functions (mPSFs) for each subregion filter mosaic, acquired at a specific position angle, in the GOODS-N and GOODS-S fields. The STPSF code ([M. D. Perrin et al. 2014](#)) is used to simulate PSFs for each filter and at a given position angle. These simulated PSFs are tiled on a pattern across the sky, embedded appropriately into exposures arrayed at the locations at the actual exposures that comprise each subregion mosaic, and then combined using the `jwst` pipeline as described in J26. The resulting simulated, noiseless subregion mosaics consist of a grid of carefully placed stars with the same dither pattern as the observed program subregion mosaics. The mPSF for each subregion mosaic is then measured from these simulated stars using the `EPSFBuilder` methods from the `photutils` package in a manner similar to that used for the HST ePSFs, but with exact known locations and without noise. The resulting mPSFs are then circularly apodized as described in Section 5.1. For GOODS-S, there are 384 distinct subregion NIRCam filter mosaic mPSFs. For GOODS-N, there are 169 distinct subregion NIRCam filter mosaic mPSFs. These distinct mPSFs are all used for common-PSF image generation (see Section 6 below), but for aperture corrections for convenience we select a single mPSF in each filter to use. For GOODS-S, we select mPSFs from the `jw012100`, `jw012860`, `jw019630`, and `jw032150` subregion mosaic mPSFs, and in GOODS-N we select from the `jw011810.hst`, `jw025140.gn_pa133`, `jw018950` subregion mosaic mPSFs, depending on the filter.

As discussed by both J26 and [Z. Ji et al. \(2024\)](#), this method produces an mPSF that reproduces extremely well the encircled energy curves measured directly from stars in mosaic images while maintaining the diffraction spike structure that can be difficult to measure at low signal-to-noise for a large number of stars in an observed mosaic.

5.4. *MIRI Point Spread Functions*

To compute aperture corrections for the JWST/MIRI photometry, we adopt the MIRI PSFs from [S. Alberts et al. \(2024\)](#). The F560W and F770W PSFs (A. Gaspar, private communication) are empirical and use high-SNR JWST commissioning observations that highlight the “cruciform” feature induced by internal reflection in the detector ([A. Gáspár et al. 2021](#); [M. Libralato et al. 2024](#); [D. Dicken et al. 2024](#)). The longer wavelength MIRI PSFs (F1000W-F2550W) are modeled using STPSF ([M. D. Perrin et al. 2014](#)). Each MIRI PSFs is resampled at the JADES DR5 mosaic resolution (0.03” pixels) and apodized as described in Section 5.1.

6. COMMON PSF MOSAICS

With the definitions of the effective point spread functions for each filter, as described in Section 5, the process for creating common-PSF images can then proceed. Our approach for generating common-PSF images is informed

by the structure of the JWST PSF, which famously features prominent diffraction spikes. Given that the mosaics involve stacks of subregion mosaics acquired at a variety of position angles, applying a common convolutional kernel to the final mosaic stack in generating a common PSF image could lead to additional artifacts related to the diffraction spikes. Correspondingly, we build common-PSF images for subregion mosaics in each filter at separate position angles by constructing a convolutional kernel using the apodized, two-dimensional PSF image appropriate for that region, and then stack the common-PSF subregion mosaics into a global common-PSF mosaic for each filter. The exceptions to this approach are the HST mosaics, for which we use realigned versions of the HLF mosaics that are constructed from HST subimages with a variety of effective PSFs. In generating our common-PSF images, we bring each filter to the F444W PSF, leaving all redder JWST NIRCam and MIRI images with their native PSFs. For the long-wavelength NIRCam filters, the subregion mosaics are processed for each NIRCam detector module as separate subregion mosaics, since each detector module has a slightly different PSF in each filter. In the JADES DR5 catalogs, properties measured on the common-PSF images are designated with a `.CONV` suffix.

Procedurally, the common-PSF images are constructed using a series of operations on the subregion filter mosaics. These subregion mosaics are prepared by splitting them into portions with appropriate zero padding to allow for rapid GPU-accelerated convolutions. This optimization was primarily necessitated by bringing the HLF mosaics to a common PSF with the JWST mosaics, as those images have the full mosaic pixel footprint in memory. The circularly-apodized versions of the native PSF of the input image and the target F444W PSF are prepared for convolutions with the subregion mosaic, which may involve padding to an optimal size for rapid convolution.

The common-PSF images are then generated by computing a convolutional kernel that deconvolves the original subregion mosaic using the input PSF, and then convolves the result with the target F444W PSF after regularizing the image with a small level of power from white noise (i.e., the variance of a white-noise random process). If the input data is y of size $K \times M$, we can define

$$S_y = \frac{|\tilde{y}|^2}{KM}, \quad (11)$$

which provides the power spectrum of the image. In the presence of Poisson noise, some fraction of this power will be contributed by a constant flat power spectrum N_y , which will correspond to the variance of the typical Poisson background. Denoting the input filter PSF as H_{in} , the regularized deconvolution kernel can be approximated as

$$\tilde{G} = \frac{\tilde{H}_{\text{in}}^*(S_y - N_y)}{|\tilde{H}_{\text{in}}|^2(S_y - N_y) + N_y} \quad (12)$$

To convolve the image to the target output PSF H_{out} , we compute

$$\tilde{y}' = \tilde{H}_{\text{out}} \tilde{G} \tilde{y} \quad (13)$$

and then take the inverse Fourier transform to find the common-PSF image y' .

We further filter each common-PSF image with a 2D cosine bell window function $B(\alpha)$ multiplied in frequency space, using the `photutils` implementation to create the filter and GPU acceleration to perform the convolution. Smaller values of the argument α correspond to low-pass filtering of the image, such that frequencies greater than α times the Nyquist frequency are suppressed. For HST ACS images, we use $\alpha = 0.3$. For HST WFC3 images, we set $\alpha = 0.4$. For the JWST NIRCam common-PSF mosaics, the value $\alpha = 0.9$ has a limited effect on the output mosaics and is intended to help reduce numerical noise in regions where the PSF matching is imperfect.

7. DATA QUALITY AND CONTEXT FLAGGING

The increasing large volume of data imaging and catalog products available from JADES and similar surveys can provide a challenge for the rapid analysis and understanding of galaxy populations. By providing additional catalog-level information on the local image data quality near objects, endeavoring to propagate consistent source information across versions of our reductions, and informing the user about the visual scene around sources of interest through context flags, we have attempted to make the catalog data more readily useful without having to analyze the much larger volume of image mosaics. This section describes some of these methods and data quality flagging provided in the catalogs.

7.1. *Source ID Restoration*

The complex evolution of the upstream data processing of the JWST imagery, the constant addition of data from new programs, and the desire to maintain consistent designations for hundreds of thousands of objects across multiple

versions of input datasets has required the development of techniques to propagate object source identifications using pixel-level information rather than catalog matching. Since the JWST images are crowded in deep imagery and the deblending algorithms can successfully disentangle complicated, multi-component projected systems, relying on catalog-level source matching based on coordinate proximity can become unreliable even when the same algorithm is applied to different reductions of the same dataset. For instance, with new data added between different reductions of mosaics in the same field either the detection or deblending images, or both, may change in a manner that alters the character of the segmentation map. A choice then has to be made as to how to propagate a source identification from one version of the reduction to the next.

Here, we choose directly to propagate source identification based on the largest number of shared pixels between segments across different versions of the reduction. Beginning with a reference segmentation map from a prior version of the reduction and the segmentation map from the current version of our processing, we create a pixel-aligned reference segmentation map on the same `WCS` header as the current version. Then, for every object, the detection catalog generated from the current version’s segmentation map is used to extract the bounding box of the object’s segment. The pixels corresponding to this segment are inspected in the reference segmentation map from the prior version, and any source ID values are recorded. The segments for each of these source IDs in the reference segmentation map are then examined in the current version’s segmentation map, and the current version segments that inherit the most pixels from a given reference segment also inherit its source identification. Any segment in the current reduction’s segmentation map whose corresponding reference segmentation source ID has been assigned to another object is instead assigned a new source ID in the new version, and usually such objects correspond to a newly deblended object.

While this pixel-level source ID restoration usually works well, there are limitations. When applied across multiple successive versions of reductions, if objects are deblended, reblended, and deblended again, their source IDs are not guaranteed to propagate unless the source ID restoration method is applied iteratively. As with proximity-based catalog-matching, the method can encounter difficulty in regions with large numbers of spurious objects from systematic noise sources (e.g., regions heavily affected by the “weave”, see J26). We plan to explore ameliorations for these issues in future work.

7.2. *Bad Pixel Flagging*

For each object, local pixel-level information about the single-band mosaics recorded in the catalogs can help provide simple quality assurance and sample filtering. Indicating whether a source could be affected by bad or missing data directly in its segmentation would be useful, but additional context for being *near* missing or bad data can also assist in identifying potential systematic uncertainties such as enhanced noise near the edge of a detector boundary or a source truncated by a chip gap. In these latter cases, the source itself may not show any bad pixels or missing data within its segmentations if simply because its segmentation may not extend into a region without data. To enable some additional context flagging, for every filter (e.g., F090W) we define a flag (e.g., `FLAG_F090W`) that records the number of bad or missing pixels in a region consisting of the bounding box for each object’s segmentation extended by 10 pixels in each direction. Defining the bad pixel flag in this manner for each object for each filter enables the end user to employ quantitative cuts based on a tolerance for potential bad or missing pixels. By comparing the value of the flag with the size of the object’s segmentation bounding box plus frame, the severity of the bad or missing data in each filter can be assessed directly from the catalog information.

7.3. *Bright Neighbors*

At the catalog level, information about relative brightness of proximate objects can provide useful context about a source’s photometric properties. For instance, a compact, faint source near a substantially brighter neighbor may have a less reliable background subtraction or photometric redshift than an isolated object. Such systematic uncertainties can be difficult to quantify directly in the photometric uncertainties, but can be captured qualitatively with context flagging. Correspondingly, we implement a bright neighbor flag (`FLAG_BN`) for each object that indicates whether any proximate source has a Kron flux at least twice larger than the primary source (`FLAG_BN= 1`) or ten times larger (`FLAG_BN= 2`). To determine whether to set `FLAG_BN`, the bounding box of each object’s segmentation is extended by 10 pixels (0.3”) in each direction and inspected for the presence other proximate sources. If the Kron flux of the proximate sources exceeds a factor of two or ten, `FLAG_BN` is set accordingly.

7.4. Parent Segmentation Identification

For each deblended object in the catalog, the relation between the object and its fully blended parent detection segment is recorded and retained as the object’s `PARENT_ID`. The `PARENT_ID` can be used to provide spatial context for objects in the catalog in tasks such as associating satellite and parent galaxies, identifying objects that may be merging, or analyzing gravitational lens systems. First, note that the parent detection segmentation map and the deblended segmentation map have the same shape and are pixel-aligned. Then, to determine an object’s `PARENT_ID` from its blended parent segmentation, the pixels covering the blended parent segment are extracted from the deblended segmentation map, and their unique values determined and counted. The deblended object ID that comprises the most pixels of the blended parent segment becomes the `PARENT_ID` for all objects deblended from that parent segment. In effect, the ID of largest object in pixel area among deblended subregions from a given blended segment is assigned as the `PARENT_ID` for all its deblended siblings.

7.5. JWST Program Bithash

The JADES DR5 products include an integer image that hash encodes which JWST programs contribute data to every pixel in the imaging data. The method for generating the program bithash is detailed in J26, and involves assigning each subregion mosaic a bit in a binary representation of the integer that indicates whether the program contributes data to a given pixel. The value of the integer hash at the location of every source in the JADES DR5 catalogs is measured and recorded in the source’s `PID_HASH` field. By decoding the `PID_HASH` to generate the list of contributing programs at the object’s location, the origin of the data can be cited appropriately. When using the JADES DR5 catalogs, we encourage use of the `PID_HASH` to find the original references for contributing data and more readily enable their citations. A full list of contributing programs, the bits assigned to each program, and the original references to the data are provided in J26.

8. PHOTOMETRIC UNCERTAINTY FRAMEWORK

The uncertainties associated with the source photometry should be comprised of the sky background and Poisson uncertainty from the electronic signal of the source flux. While the latter contribution can be computed directly from the integrated source flux and the calibrated gain of the detector, the sky background has to be modeled owing to pixel-level correlations induced during the mosaicing process. Dithering of exposures and the combination of subregion mosaics at differing position angles causes resampling of pixels during the construction of the mosaics, and the individual exposure pixel values become coupled across multiple pixels in the final mosaics. These correlations are complicated by the character of the JWST PSF, with large-angle diffraction spikes, and even by the JWST detector interpixel capacitance (B. J. Rauscher et al. 2014).

As a result of the pixel-level correlations, the scaling of photometric uncertainty from the sky background with the size of an aperture used to integrate the source flux should scale superlinearly with the size of the aperture (e.g., I. Labb   et al. 2005; R. Quadri et al. 2007; K. E. Whitaker et al. 2011; R. E. Skelton et al. 2014; K. E. Whitaker et al. 2019). The scaling of the uncertainty with the linear aperture size can be approximately modeled with a power-law as

$$\sigma = \sigma_1 N^\beta \quad (14)$$

where N is the linear aperture size in pixels, σ_1 is the single-pixel uncertainty, and $1 \leq \beta \leq 2$ characterizes the pixel covariance through the increase of uncertainty with aperture size and is bounded between uncorrelated ($\beta = 1$) and perfectly correlated ($\beta = 2$) limits. Since the correlations arise from details of the image combination process, the local number, relative orientation on the sky, and the composite dither pattern of the exposures will affect the value of β spatially. We therefore expect the relation expressed in Equation 14 to vary spatially throughout the image. The degree of inhomogeneity of the mosaic pattern and depth will in turn affect the level of spatial variation in the correlations. Assuming a uniform sky, if the mosaic is fairly homogeneous, the distribution of random aperture fluxes measured on source-free regions of the sky will also be fairly uniform across the mosaic. The scaling in Equation 14 can be computed by measuring an outlier-insensitive estimate of the spread of random aperture fluxes, such as the mean absolute deviation estimator for the normal distribution standard deviation, as a function of aperture size and then fitting the resulting trend. The fit can be used to assign model photometric uncertainties to flux measurements made using different aperture sizes. This same method can be used to compute the photometric uncertainties for sources in common-PSF mosaics, which will have a different pixel covariances and associated β values compared with their corresponding native PSF mosaics.

For a more complicated mosaic that is inhomogeneous in depth and composition, instead of a dominant trend of uncertainty with aperture size there will be a variety of subtrends. The degree of pixel covariance will be a local quantity. In [M. J. Rieke et al. \(2023\)](#), the uncertainty scaling Equation 14 was measured for the `jw01180.deep` and `jw019630` subregion mosaics by measuring the sky flux in random apertures across the image and grouping the apertures by the local exposure time. Many uncertainty scalings were estimated, and the photometric uncertainties for a given source were assigned from these fitted scalings based on the exposure time at the source location and the aperture used for photometry (see their Figure 3). The same technique was used in previous JADES imaging data releases and analyses, where the combined mosaics were not highly inhomogeneous in depth or composition (e.g., [D. J. Eisenstein et al. 2025](#); [F. D'Eugenio et al. 2025a](#); [B. Robertson et al. 2024](#)).

For the current analysis, as described by J26, the JADES DR5 data release mosaics display dramatic variations in depth and composition in their exposures. As the bithash images presented in J26 indicate, the transition between regions with substantial depth or composition variation can be quite sharp and the character of the pixel covariance could be expected to change discontinuously. These features suggest that the approach of fitting a trend of uncertainty with aperture size, or even fitting multiple trends of uncertainty with aperture size conditioned on the local mosaic properties, should be adapted for a more complex mosaic pattern. Here we introduce such an approach. First, mosaics of the uncertainty measured from the distribution of local sky flux measured in random apertures are constructed for each filter and for a range of aperture sizes (Section 8.1). We then present a regression method for creating a model of the photometric uncertainty at each pixel location in our mosaics as a function of aperture size, which uses the background variance mosaic propagated from the `jwst` pipeline as a spatial template for the single-pixel uncertainty and jointly fits to the random aperture uncertainty mosaics as a power-law with increasing aperture size (Section 8.2).

8.1. *Uncertainty Mosaics*

The uncertainty mosaics provide a map of the local spread in sky flux values measured in apertures randomly placed across the image. To create the uncertainty mosaics, we begin by selecting a low resolution grid of pixel locations where the local uncertainty will be estimated at a 50:1 ratio relative to the full mosaic resolution. We then distribute across each filter mosaic 4,000,000 random apertures at valid locations masked by the detection segmentation map and where the filter $WHT > 1$. A KDTree is built using the `scipy` library and used to search for a target of 1000 nearest neighbor aperture locations to each pixel location where the local sky background distribution will be estimated. In the tree search, we use a bithash mosaic constructed for each filter individually to inform which random apertures have been drawn from regions that have the same combination of subregion mosaics and are therefore likely to show the same depth and pixel covariance properties. We prioritize random aperture locations from the same bithash as the pixel location of interest in targeting a 1000 neighbors, but if at least 500 neighbor apertures cannot be selected from the same bithash value (e.g., the pixel is near a border between subregion mosaics) then we augment those apertures with the nearest random sky apertures of any bithash value. The RMS of these random sky fluxes are measured and recorded, and then the low resolution uncertainty mosaic is reinterpolated to the full resolution of the DR5 mosaic using the GPU-accelerated `cupy` implementation of the `scipy.ndimage.zoom` routine. Any pixel-level interpolation errors (zeros or negative errors) are replaced with the median valid uncertainty mosaic value from the surrounding 21×21 pixel footprint. Uncertainty mosaics are generated for circular apertures with radii $r = [0.1'', 0.15'', 0.25'', 0.3'', 0.35'', 0.5'', 0.9'', 1.5'']$ for every native resolution and common-PSF filter mosaic.

8.2. *Regression Model for Uncertainty Mosaics*

With the uncertainty mosaics computed, an extension of the power-law scaling model Equation 14 can be constructed for every pixel. Indeed, for the HST and MIRI mosaics we fit simple power-laws at the pixel level throughout the mosaic to compute model uncertainty mosaics at aperture sizes of $r = [0.1'', 0.15'', 0.25'', 0.3'', 0.35'', 0.5'']$. For smaller apertures, we extrapolate the power-law toward the single-pixel limit ($0.03''$). Mosaics of the power-law amplitude and index β are retained. For larger apertures we scale linearly from the $r = 0.5''$ value as the pixel covariances begin to decorrelate on larger scales.

For the NIRCam mosaics, we can additionally leverage the computation of the pixel-level source-free background uncertainty image, which is stored in the WHT HDU as described in J26. This mosaic quantity replaces the WHT value from the standard `jwst` pipeline data model and represents the expected pixel-level uncertainty in the final associated with the quadrature sum of read and sky background noise. While we expect this image to not perfectly reflect the true amplitude of the pixel-level background, it does correctly encode the relative expected depths of the pixel-level

background associated with the various subregions of the mosaic and the discontinuity of their spatial topology. We therefore wish to include this pixel-level uncertainty as a template for the single-pixel uncertainty mosaic, allowing for rescaling by a multiplicative coefficient $\exp(\alpha)$, and then perform a joint fit of the coefficient and all the power-law indices β_j for the pixel-by-pixel uncertainty scalings. Given a number of m pixels in the mosaic, this template-based fitting of the uncertainty model for NIRCam ($m+1$ parameters) is much more constrained than for the HST and MIRI mosaics ($2m$ parameters). The fit of a single value for α does couple the uncertainty scaling of all pixels together, although somewhat weakly. Since we newly introduce this method here, below we explicitly work through the analytical solution of the system of equations for α and β_j . Readers interested in the utilization of the uncertainties in the forced photometry of sources can find the related discussion in Section 9.

Consider the mosaic with m pixels labeled with pixel index j , each with n aperture RMS measurements labeled with aperture index i . A model for the uncertainty scaling with the linear aperture sizes N_{ij} for every pixel location based on a single-pixel aperture template can be written as

$$\sigma_{ij} = AP_j N_{ij}^{\beta_j} \quad (15)$$

where AP_j provides the single-pixel RMS, A is a multiplicative coefficient common to every pixel, P_j is the template for the RMS uncertainty for a single-pixel aperture, and the $1 \leq \beta_j \leq 2$ are power-law indices. Taking the logarithm of both sides, the model can be written as

$$y_{ij} = p_j + \alpha + \beta_j x_{ij} \quad (16)$$

where $\alpha = \log A$, $p_j = \log P_j$, $x_{ij} = \log N_{ij}$ and $y_{ij} = \log \sigma_{ij}$. The goal then is to compute best fit values of α and β_j that best reproduce y_{ij} for each x_{ij} .

The summed squared difference between the model and the measured RMS uncertainties can then be written

$$\chi^2 = \sum_j^m \sum_i^n [y_{ij} - (p_j + \alpha + \beta_j x_{ij})]^2 \quad (17)$$

where i runs over the number of n apertures, and j runs over the number of pixels p_j in the template. The metric χ^2 can be minimized with respect to the parameters α and β_j by taking partial derivatives

$$\frac{\partial \chi^2}{\partial \alpha} = 2 \sum_j \sum_i [y_{ij} - (p_j + \alpha + \beta_j x_{ij})](-1) = 0 \quad (18)$$

and

$$\frac{\partial \chi^2}{\partial \beta_j} = 2 \sum_i [y_{ij} - (p_j + \alpha + \beta_j x_{ij})](-x_{ij}) = 0 \quad (19)$$

After noting that $\sum_i \sum_j \alpha = n m \alpha$, the system of equations can be written as a matrix equation

$$\mathbf{M} \vec{\phi} \equiv \begin{bmatrix} \Sigma_i x_{i1}^2 & 0 & \cdots & 0 & \Sigma_i x_{i1} \\ 0 & \Sigma_i x_{i2}^2 & \ddots & \vdots & \vdots \\ \vdots & \ddots & \ddots & \vdots & \vdots \\ 0 & \cdots & \cdots & \Sigma_i x_{ij}^2 & \Sigma_i x_{ij} \\ \Sigma_i x_{i1} & \cdots & \cdots & \Sigma_i x_{ij} & nm \end{bmatrix} \begin{bmatrix} \beta_1 \\ \vdots \\ \beta_j \\ \vdots \\ \alpha \end{bmatrix} = \begin{bmatrix} \Sigma_i x_{i1} (y_{i1} - p_1) \\ \vdots \\ \vdots \\ \Sigma_i x_{ij} (y_{ij} - p_j) \\ \Sigma_j \Sigma_i (y_{ij} - p_j) \end{bmatrix} \equiv \vec{z} \quad (20)$$

The system can be solved for the parameters $\vec{\phi} = [\beta_j, \alpha]$ by inverting the left-most matrix \mathbf{M} , whose block-like structure makes an analytical solution feasible. The solution for the parameters is then just $\vec{\phi} = \mathbf{M}^{-1} \vec{z}$.

The matrix \mathbf{M} can be split into a block-wise form as

$$\mathbf{M} = \begin{bmatrix} \mathbf{A} & \mathbf{B} \\ \mathbf{C} & \mathbf{D} \end{bmatrix} \quad (21)$$

where

$$\mathbf{A} = \begin{bmatrix} \Sigma_i x_{i1}^2 & 0 & \cdots & 0 \\ 0 & \Sigma_i x_{i2}^2 & \ddots & \vdots \\ \vdots & \ddots & \ddots & 0 \\ 0 & \cdots & \cdots & \Sigma_i x_{ij}^2 \end{bmatrix}, \quad \mathbf{B} = \begin{bmatrix} \Sigma_i x_{i1} \\ \vdots \\ \Sigma_i x_{ij} \end{bmatrix}, \quad \mathbf{C} = \begin{bmatrix} \Sigma_i x_{i1} & \cdots & \Sigma_i x_{ij} \end{bmatrix}, \quad \mathbf{D} = \begin{bmatrix} nm \end{bmatrix}. \quad (22)$$

The inverse of this matrix is computable because \mathbf{A} is diagonal and \mathbf{D} is a scalar constant. Note that $\mathbf{B} = \mathbf{C}^T$, but each submatrix is treated distinctly for clarity. The blockwise inverse is complicated but analytical, and can be written as

$$\mathbf{M}^{-1} = \begin{bmatrix} \mathbf{A}^{-1} + \mathbf{A}^{-1}\mathbf{B}(\mathbf{M}/\mathbf{A})^{-1}\mathbf{C}\mathbf{A}^{-1} & -\mathbf{A}^{-1}\mathbf{B}(\mathbf{M}/\mathbf{A})^{-1} \\ -(\mathbf{M}/\mathbf{A})^{-1}\mathbf{C}\mathbf{A}^{-1} & (\mathbf{M}/\mathbf{A})^{-1} \end{bmatrix} \quad (23)$$

where

$$\mathbf{A}^{-1} = \begin{bmatrix} (\Sigma_i x_{i1}^2)^{-1} & 0 & \cdots & 0 \\ 0 & (\Sigma_i x_{i2}^2)^{-1} & \ddots & \vdots \\ \vdots & \ddots & \ddots & 0 \\ 0 & \cdots & \cdots & (\Sigma_i x_{ij}^2)^{-1} \end{bmatrix} \quad (24)$$

is simple because \mathbf{A} is diagonal, and

$$\mathbf{M}/\mathbf{A} = \mathbf{D} - \mathbf{C}\mathbf{A}^{-1}\mathbf{B}. \quad (25)$$

Note that \mathbf{M}/\mathbf{A} is actually a scalar constant, so $(\mathbf{M}/\mathbf{A})^{-1}$ is also a scalar constant. The quantity

$$\mathbf{C}\mathbf{A}^{-1}\mathbf{B} = \sum_j \frac{(\Sigma_i x_{ij})^2}{\Sigma_i x_{ij}^2} \quad (26)$$

expresses ratio of square of the summed logarithmic aperture sizes to the sum of their squares, totaled over the mosaic. This scalar is then subtracted from \mathbf{D} , and the inverse taken to provide the lower-right submatrix inverse

$$(\mathbf{M}/\mathbf{A})^{-1} = [\mathbf{D} - \mathbf{C}\mathbf{A}^{-1}\mathbf{B}]^{-1} = \left[nm - \sum_j \frac{(\Sigma_i x_{ij})^2}{\Sigma_i x_{ij}^2} \right]^{-1}. \quad (27)$$

The submatrix $(\mathbf{M}/\mathbf{A})^{-1}$ is used to compute the upper right and lower left submatrices as

$$-\mathbf{A}^{-1}\mathbf{B}(\mathbf{M}/\mathbf{A})^{-1} = - \left[nm - \sum_j \frac{(\Sigma_i x_{ij})^2}{\Sigma_i x_{ij}^2} \right]^{-1} \begin{bmatrix} \frac{\Sigma_i x_{i1}}{\Sigma_i x_{i1}^2} \\ \vdots \\ \frac{\Sigma_i x_{ij}}{\Sigma_i x_{ij}^2} \end{bmatrix} \quad (28)$$

and

$$-(\mathbf{M}/\mathbf{A})^{-1}\mathbf{C}\mathbf{A}^{-1} = - \left[nm - \sum_j \frac{(\Sigma_i x_{ij})^2}{\Sigma_i x_{ij}^2} \right]^{-1} \begin{bmatrix} \frac{\Sigma_i x_{i1}}{\Sigma_i x_{i1}^2} & \cdots & \frac{\Sigma_i x_{ij}}{\Sigma_i x_{ij}^2} \end{bmatrix} \quad (29)$$

The remaining upper left submatrix in Equation 23 for \mathbf{M}^{-1} is the sum of \mathbf{A}^{-1} (Equation 24) and the matrix product of Equations 25, 28, and 29.

Once the best-fit parameters α and β_j are determined, uncertainty model mosaics are computed for every filter and circular aperture size $r = [0.1'', 0.15'', 0.25'', 0.3'', 0.35'', 0.5'']$. The sky background contribution to the photometric uncertainty of each object is then log-linearly interpolated based on the aperture size of the photometric measure and the object's position on the uncertainty model mosaic. These uncertainties are added in quadrature with the Poisson uncertainty associated with the electronic signal of the source, and reported as the uncertainties with the ‘_e’ suffixes in the released photometric catalogs. We also measure the uncertainty estimates from the `ERR` HDU from the `jwst` pipeline as the uncertainties with the ‘_ei’ suffixes in the catalogs, noting that these ‘_ei’ uncertainties do not account for possible correlated pixel affecting the uncertainty scaling with aperture size and therefore underestimate the photometric uncertainties.

9. FORCED PHOTOMETRY

The source population in the JADES images display a wide range of spectral energy distributions. The approach to measuring photometry for sources involves the forced sum of pixel values within apertures centered at the locations of detections, where the detected sources are discovered in deep long-wavelength stacks where the sensitivity to many sources is expected to be high. By performing forced photometry for detections from the long-wavelength stack, high-redshift sources can be discovered even as their fluxes in dropout filters approach the sky background.

In this Section, we describe fixed aperture forced photometry including circular aperture photometry (Section 9.1) and ellipsoidal Kron aperture photometry (Section 9.2), where the aperture size is selected or determined from the source properties in the detection image. Section 10 below describes curve-of-growth photometric measures for every object. We note here that when using the forced photometry on unconvolved mosaics for scientific applications, the use of a fixed aperture with point source aperture corrections will induce anomalous colors for extended objects. Analyses that want unbiased colors (for objects with no intrinsic color gradients) should use the common-PSF mosaics. Analyses that want maximum SNR for compact objects and in particular maximum SNR on the measurement of differences in flux between nearby bands should use photometry performed on the unconvolved mosaics.

9.1. Circular Aperture Photometry

For every source, forced circular aperture photometry is reported for apertures of radii $r = [0.1'', 0.15'', 0.25'', 0.3'', 0.35'', 0.5'']$. These photometric measures are labeled as CIRC1-CIRC6 in the catalogs, with the filter of the measurement included as a prefix. For instance, the $r = 0.3''$ circular aperture measurements for the F090W filter are labeled as F090W_CIRC4. The photometry is aperture corrected by measuring the fractional encircled energy of the corresponding filter’s PSF within the aperture (see Section 5). For each filter, an additional circular aperture photometric measure CIRC0 is computed within a radius that encircles 80% of the PSF energy for that band, such that the aperture correction for a point source should be constant with wavelength. The photometric uncertainties computed from the model regression on the random aperture uncertainty mosaics, as described in Section 8, are reported with the `_e` suffix (e.g., these F090W uncertainties are F090W_CIRC4`_e`) and the uncertainties estimated from the ERR HDU are labeled with the `_ei` suffix (e.g., F090W_CIRC4`_ei`). The forced circular aperture photometry is reported for the filter and common-PSF mosaics in the CIRC and CIRC_CONV HDUs of the catalogs, respectively.

We include photometry on the direct images and also include corrections for a local background. For circular aperture photometry, the local background is measured in a circular annulus over the radii $1.5'' < r < 1.55''$. As with the source flux measurement, pixels from segmentations belonging to other sources are censored. The median pixel value within the annulus is computed, and then the corresponding interior flux within the circular aperture area is subtracted from the integrated flux measurement. The background flux removed is recorded in the field labeled with the `_bkg` suffix (e.g., F090W_CIRC1`_bkg`). The circular aperture measurements that include background subtraction are provided in the CIRC_BSUS and CIRC_BSUS_CONV HDUs of the catalogs.

Figure 4 presents histograms of the JADES DR5 catalog sources with $\text{SNR} > 5$ $r = 0.1''$ circular aperture fluxes in each of the 35 HST/ACS, HST/WFC3, JWST/NIRCam, and JWST/MIRI filter mosaics used in this work, spanning a factor of $\sim 60\times$ in wavelength. Each panel shows the source count histograms for the GOODS-N (blue) and GOODS-S (red) fields, plotted over the range of $31 > m_{AB} > 15$. The number of $\text{SNR} > 5$ sources range from $N > 300,000$ in F200W, F277W, and F356W across GOODS-S and GOODS-N to only $N = 127$ in F2550W (from SMILES). The GOODS-S and GOODS-N source counts are consistent once the areal filter coverage is considered.

Given the release of prior photometric catalogs by the JADES collaboration, a comparison between source photometric measures between catalog versions is warranted. Figure 5 presents a direct comparison between the JADES DR3 photometric catalog for GOODS-N released by F. D’Eugenio et al. (2025a) and the JADES DR5 photometric catalog described in this work. Shown are the differences between the DR3 CIRC1 photometry and the DR5 CIRC1 photometry, plotted as a fraction change in flux relative to the DR5 CIRC1 photometry, as a function of the DR5 CIRC1 AB magnitude in the F090W, F115W, F150W, F200W, F277W, F335M, F356W, F410M, and F444W JWST NIRCam filters. Differences are measured for sources whose centroids match between catalogs better than the CIRC1 aperture size of $r = 0.1''$ and have $\text{SNR} > 5$ in DR5. Normalized two-dimensional histograms of these histograms are presented (shaded regions) along with running windowed medians (blue lines). The median value of the running median differences for each filter are reported in the image panels. Typically, measured flux differences are better than 1% with the largest differences in F090W.

Table 2. Circular Aperture Size and Correction Information

| Filter | CIRC0 | | CIRC1, $r = 0.1''$ | CIRC2, $r = 0.15''$ | CIRC3, $r = 0.25''$ | CIRC4, $r = 0.3''$ | CIRC5, $r = 0.35''$ | CIRC6, $r = 0.5''$ |
|-------------------|--------------|-------------|--------------------|---------------------|---------------------|--------------------|---------------------|--------------------|
| | r [arcsec] | Aper. Corr. | Aper. Corr. | Aper. Corr. | Aper. Corr. | Aper. Corr. | Aper. Corr. | Aper. Corr. |
| HST/ACS F435W | 0.433 | 1.25 | 1.532 | 1.277 | 1.161 | 1.141 | 1.128 | 1.100 |
| HST/ACS F606W | 0.592 | 1.25 | 1.628 | 1.304 | 1.181 | 1.151 | 1.134 | 1.104 |
| HST/ACS F775W | 0.769 | 1.25 | 1.620 | 1.285 | 1.166 | 1.140 | 1.116 | 1.088 |
| HST/ACS F814W | 0.806 | 1.25 | 1.667 | 1.312 | 1.165 | 1.139 | 1.115 | 1.082 |
| HST/ACS F850LP | 0.904 | 1.25 | 2.067 | 1.522 | 1.259 | 1.218 | 1.185 | 1.123 |
| HST/WFC3 F105W | 1.055 | 1.25 | 2.772 | 1.738 | 1.266 | 1.209 | 1.181 | 1.120 |
| HST/WFC3 F125W | 1.249 | 1.25 | 2.955 | 1.865 | 1.305 | 1.222 | 1.185 | 1.132 |
| HST/WFC3 F140W | 1.392 | 1.25 | 3.100 | 1.954 | 1.357 | 1.251 | 1.203 | 1.152 |
| HST/WFC3 F160W | 1.537 | 1.25 | 3.309 | 2.064 | 1.413 | 1.277 | 1.210 | 1.153 |
| JWST/NIRCam F070W | 0.161 | 1.25 | 1.355 | 1.267 | 1.144 | 1.114 | 1.095 | 1.060 |
| JWST/NIRCam F090W | 0.141 | 1.25 | 1.319 | 1.240 | 1.156 | 1.122 | 1.101 | 1.066 |
| JWST/NIRCam F115W | 0.129 | 1.25 | 1.296 | 1.226 | 1.155 | 1.130 | 1.118 | 1.071 |
| JWST/NIRCam F150W | 0.125 | 1.25 | 1.324 | 1.223 | 1.152 | 1.135 | 1.128 | 1.079 |
| JWST/NIRCam F162M | 0.128 | 1.25 | 1.346 | 1.223 | 1.154 | 1.137 | 1.124 | 1.084 |
| JWST/NIRCam F182M | 0.135 | 1.25 | 1.386 | 1.225 | 1.160 | 1.137 | 1.124 | 1.091 |
| JWST/NIRCam F200W | 0.141 | 1.25 | 1.410 | 1.234 | 1.166 | 1.138 | 1.124 | 1.092 |
| JWST/NIRCam F210M | 0.147 | 1.25 | 1.430 | 1.242 | 1.173 | 1.141 | 1.124 | 1.096 |
| JWST/NIRCam F250M | 0.176 | 1.25 | 1.573 | 1.318 | 1.179 | 1.160 | 1.136 | 1.103 |
| JWST/NIRCam F277W | 0.189 | 1.25 | 1.623 | 1.351 | 1.184 | 1.166 | 1.146 | 1.105 |
| JWST/NIRCam F300M | 0.201 | 1.25 | 1.675 | 1.384 | 1.189 | 1.170 | 1.156 | 1.109 |
| JWST/NIRCam F335M | 0.221 | 1.25 | 1.762 | 1.428 | 1.206 | 1.174 | 1.162 | 1.115 |
| JWST/NIRCam F356W | 0.231 | 1.25 | 1.811 | 1.444 | 1.220 | 1.178 | 1.164 | 1.120 |
| JWST/NIRCam F410M | 0.259 | 1.25 | 1.965 | 1.488 | 1.270 | 1.196 | 1.170 | 1.139 |
| JWST/NIRCam F430M | 0.270 | 1.25 | 2.043 | 1.504 | 1.291 | 1.207 | 1.173 | 1.145 |
| JWST/NIRCam F444W | 0.275 | 1.25 | 2.062 | 1.514 | 1.299 | 1.215 | 1.176 | 1.145 |
| JWST/NIRCam F460M | 0.290 | 1.25 | 2.176 | 1.542 | 1.330 | 1.235 | 1.182 | 1.151 |
| JWST/NIRCam F480M | 0.302 | 1.25 | 2.262 | 1.567 | 1.351 | 1.254 | 1.191 | 1.152 |
| JWST/MIRI F560W | 1.334 | 1.25 | 5.945 | 3.246 | 1.989 | 1.781 | 1.638 | 1.434 |
| JWST/MIRI F770W | 0.792 | 1.25 | 5.443 | 2.901 | 1.739 | 1.609 | 1.541 | 1.341 |
| JWST/MIRI F1000W | 0.632 | 1.25 | 6.954 | 3.500 | 1.826 | 1.595 | 1.489 | 1.369 |
| JWST/MIRI F1280W | 0.756 | 1.25 | 9.964 | 4.803 | 2.218 | 1.812 | 1.596 | 1.401 |
| JWST/MIRI F1500W | 0.864 | 1.25 | 12.871 | 6.082 | 2.644 | 2.082 | 1.765 | 1.423 |
| JWST/MIRI F1800W | 1.020 | 1.25 | 17.626 | 8.180 | 3.371 | 2.564 | 2.092 | 1.509 |
| JWST/MIRI F2100W | 1.157 | 1.25 | 22.524 | 10.352 | 4.137 | 3.085 | 2.462 | 1.645 |
| JWST/MIRI F2550W | 1.159 | 1.25 | 32.483 | 15.761 | 5.697 | 4.151 | 3.227 | 1.967 |

NOTE—The JWST NIRCam circular aperture corrections are computed from the model PSFs presented by J26, while the JWST MIRI circular aperture corrections are calculated from the model PSFs presented by A26 (see Section 5). The HST aperture corrections are computed from the empirical PSFs computed in Section 5.2.

9.2. Kron Aperture Photometry

Forced ellipsoidal aperture photometry is performed about the centroid locations of every object in every filter. For the size of the apertures, to approximate a total flux we adopt the Kron aperture sizes determined from the Gaussian profile regression fits to the detection image data described in Section 4.2. The semimajor axis `A_KRON` and semiminor axis `B_KRON` of these ellipsoidal apertures are set to be proportional to the 2D Gaussian profile semimajor and semiminor sizes, times the dimensionless unscaled Kron radius `R_KRON_U` and the Kron parameter $k = 2.5$. The position angle of the ellipsoidal aperture on the sky `THETA` is computed during the Gaussian model regression and kept fixed when forcing photometry. We additionally compute “short” Kron photometry using a smaller parameter $k = 1.4$ to set the corresponding semimajor and semiminor aperture axes `A_KRON_S` and `B_KRON_S`. When measuring the photometry, a background subtraction is performed where the local background per pixel is measured from an ellipsoidal annular aperture of width 4 pixels, inner semimajor axis `2A_KRON`, and the same axis ratio as the Kron aperture. When measuring the photometry or background, pixels belonging to the segmentations of other sources are masked. The uncertainties are interpolated from uncertainty model mosaics (see Section 8.1) appropriately for the Kron aperture size of each source (`{BAND}_KRON_e` uncertainties) and also estimated from the `ERR` HDU if available. The

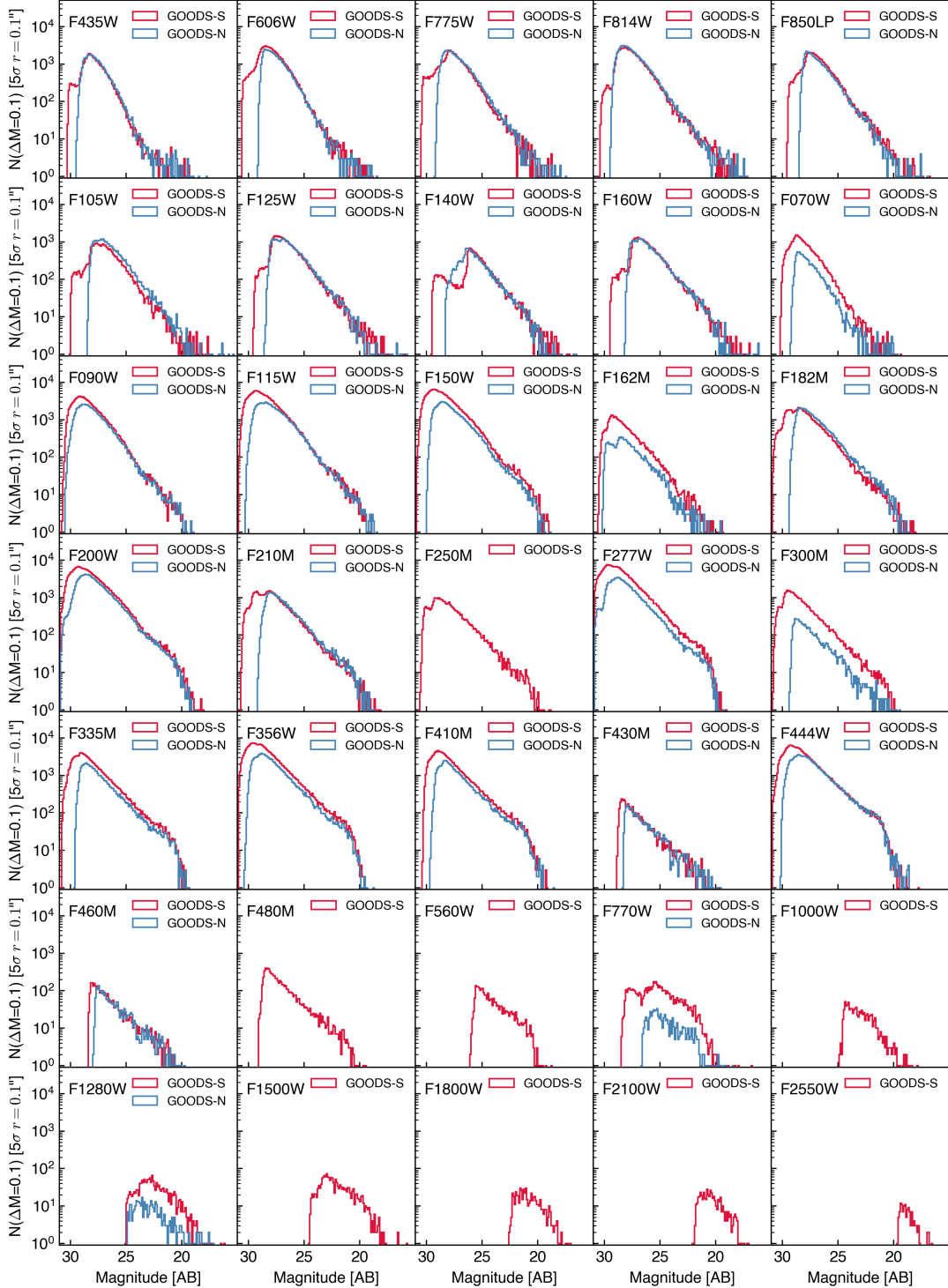


Figure 4. Histograms of the source counts for 5σ -significant objects measured in $r = 0.1''$ circular apertures, for the 35 HST/ACS, HST/WFC3, JWST/NIRCam, and JWST/MIRI filters used in the JADES DR5 photometric catalogs. Shown in each panel are the source counts in the GOODS-N (blue) and GOODS-S (red) fields in bins of width $\Delta M = 0.1$ magnitudes, and the filter mosaic measured in each panel is indicated in the upper left corner. All detected sources are considered for inclusion in each panel, but only sources with $\text{SNR} > 5$ CIRC1 photometry in a given filter are included in the histograms for that band. The source counts between GOODS-S and GOODS-N are consistent once differences in areal coverage are considered.

fluxes and uncertainties are aperture corrected by integrating the enclosed energy of the filter PSF over the ellipsoidal

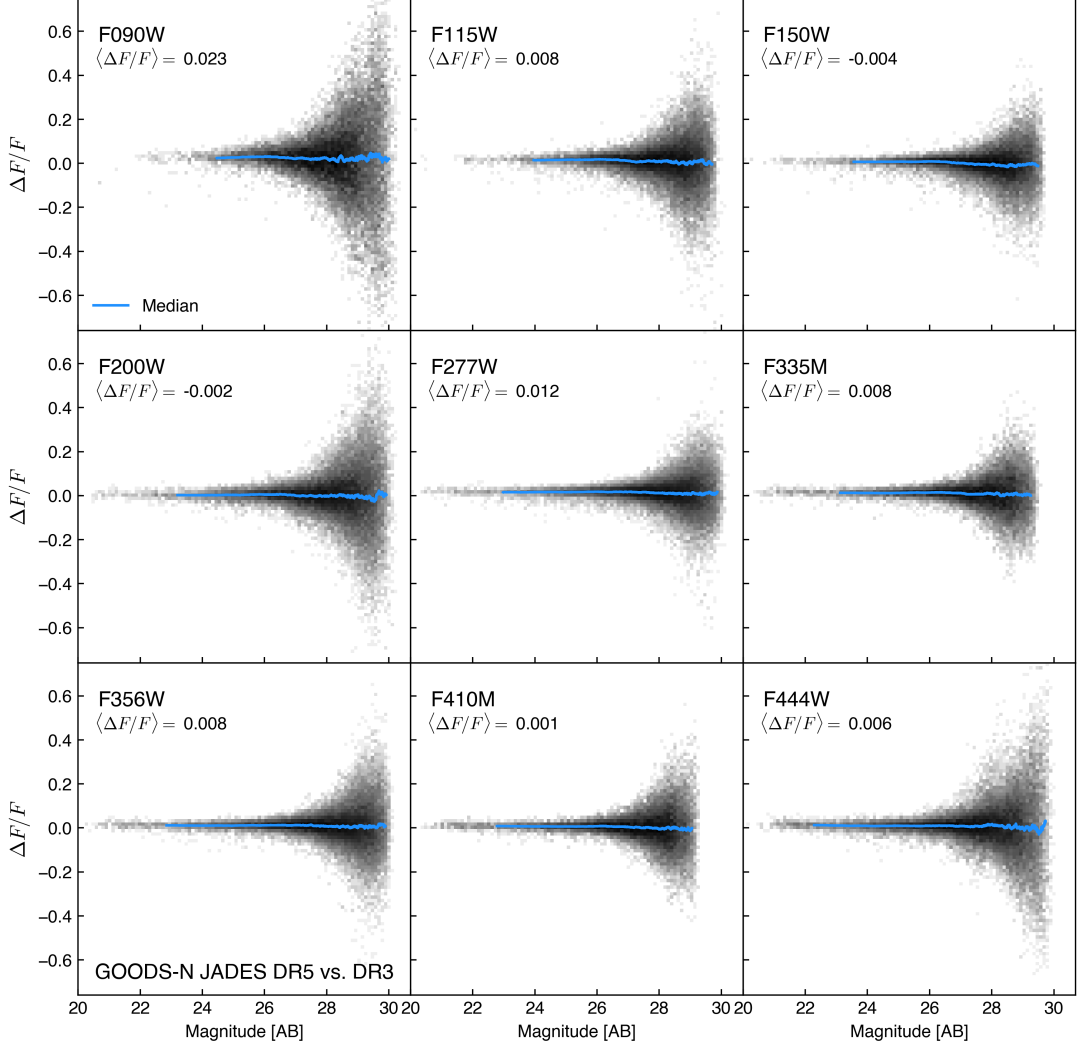


Figure 5. Comparison between the JADES DR3 vs. DR5 photometry. Shown are the fractional flux differences in F090W, F115W, F150W, F200W, F277W, F335M, F356W, F410M, and F444W between the DR3 and DR5 $r = 0.1''$ circular aperture photometry (CIRC1), measured relative to the DR5 flux, for sources with DR5 SNR > 5 in each filter, as a function of the CIRC1 AB magnitude in the filter. The distribution of flux differences are shown as normalized two-dimensional histograms (shaded regions). Running windowed medians of the histogram values are computed and reported as a blue line, and the median of the running medians is reported as an annotation in each panel. The typical flux differences between DR3 and DR5 for well-matched sources is better than 1%.

aperture of the source. The forced Kron aperture photometry is measured for every source in every filter, using both the native (`{BAND}_KRON`) and common-PSF mosaics (`{BAND}_KRON_CONV`).

10. CURVE OF GROWTH

The adoption of Kron apertures generating forced total flux estimates is heuristic but follows the previous JADES photometric releases (e.g., [M. J. Rieke et al. 2023](#); [D. J. Eisenstein et al. 2025](#); [F. D'Eugenio et al. 2025a](#)) and benefits from convenient implementations in the `photutils` library. Here we introduce a new photometric measurement for the JADES photometric catalog releases, where for every source in every filter mosaic and common-PSF image the curve-of-growth of the flux distribution is computed. The curves-of-growth are computed in ellipsoidal apertures with maximum semimajor and semiminor extent of `2A_KRON` and `2B_KRON`, respectively. This aperture defines the region within which the `FLUX_TOT` for the source is computed. Just outside these apertures, the background flux is computed and subtracted from the total interior flux within the aperture. A series of fixed separation apertures with the same axis ratio and position angle are placed within the maximum aperture size, and the aperture fluxes are computed. An

interpolation table is generated, and then the aperture sizes that enclose fractional increases of 5% of the `FLUX_TOT` are determined. The semimajor axes of these apertures are recorded as `A_5`, `A_10`, `A_15`... all the way through `A_100`, where `A_100` is the inner most aperture size that first contains a flux `FLUX_TOT`, which can be smaller than `2A_KRON` if the curve-of-growth flattens at large distance. These aperture sizes then determine the curve-of-growth as the interior flux within them grows to reach `FLUX_TOT`. The uncertainties on the `FLUX_TOT` are computed from the uncertainty mosaics for apertures the size of `A_100`, and the sky background contribution separately recorded in addition to the total uncertainty. The uncertainty estimate from the `ERR` HDU image is also measured.

Figure 6 provides an overview of the various photometric apertures used to generate the catalog entries for an example source in the JADES GOODS-S mosaic. For each source detected in the mosaics, the segmentation map (bottom left) and pixel data (upper left) are used to define the object centroid (top center) about which the Kron aperture (top center, magenta ellipse) and circular apertures (colored circles) are placed for integrating photometry. The elliptical annulus used for the background estimate located at twice the Kron aperture is also indicated (top center), and is used for background subtraction for the `KRON`, `GROWTH`, and `CIRC_BSUS` photometric measures as discussed above. The bottom middle panel shows the curve-of-growth annuli for this source, and as it first reaches its total flux `FLUX_TOT` at a distance smaller than twice the Kron aperture size the curve-of-growth apertures are placed at smaller interior distances. The background-subtracted photometric measures `CIRC_BSUS` (rainbow-colored points), Kron photometry (orchid point; plotted at a circularized distance) and the curve-of-growth (blue line; plotted at a circularized distance) are shown in the far right panel; each are consistent at a given distance from the source. We note that the curve-of-growth provides an empirical two-dimensional model for the source, and can be used as a proxy for the source integrated surface brightness profile. Measures of the light concentration can be estimated from the ratio of the curve-of-growth aperture sizes, and different estimates of the total flux can be constructed from the curve-of-growth based on how the integrated flux changes with distance. For a detailed analysis of the surface brightness profiles of JADES DR5 sources, we refer the reader to [C. Carreira et al. \(submitted\)](#). They use Bayesian methods to infer and catalog Sérsic profile ([J. L. Sérsic 1963, 1968](#)) parameters and associated uncertainties for all GOODS-N and GOODS-S DR5 sources in GOODS-N and GOODS-S in each available JWST/NIRCam wide-band filter.

11. PHOTOMETRIC REDSHIFTS

Photometric redshifts provide a valuable derived property for objects in the JADES photometric surveys. To generate photometric redshift catalogs for the JADES DR5 sources we follow closely the methods described in [K. N. Hainline et al. \(2024\)](#) and [M. J. Rieke et al. \(2023\)](#), and use the `EAZY` code ([G. B. Brammer et al. 2008](#)) to provide template-based photometric redshift estimates. We use the same template set used by [K. N. Hainline et al. \(2024\)](#) that includes the original [G. B. Brammer et al. \(2008\)](#) templates augmented with line emission, an additional dusty template from the `EAZY` suite, a high-equivalent width emission line template from [D. K. Erb et al. \(2010\)](#), and templates derived from the JAGUAR mock galaxy catalogs ([C. C. Williams et al. 2018](#)). These templates are shown in Figure 1 of [K. N. Hainline et al. \(2024\)](#). At high redshift, the effects of intergalactic medium absorption from neutral hydrogen are included in a manner consistent with the [P. Madau \(1995\)](#) model.

In using `EAZY` to compute photometric redshifts, we first compute a set of photometric offsets derived by fitting templates to the photometry of a subset of galaxies selected to have $\text{SNR} \sim 20 - 50$ in `F115W` and semimajor axes less than 5 pixels. We set an error floor on the photometry of 5%. In performing these fits to JWST/NIRCam `CIRC3` ($r = 0.25''$) photometry alone, we found that the template fits were consistent with no required rescaling of the photometry for NIRCam filters to match the SED templates as a population. This result then improves on that found in [K. N. Hainline et al. \(2024\)](#), who found typical photometric offsets of $\sim 2\text{-}5\%$ required for NIRCam filters, and may originate from the numerous subsequent improvements to the image quality and cataloging methods. Adopting no offsets for NIRCam, we then determined the photometric offsets for the HST photometry by re-fitting the HST and NIRCam data jointly with `EAZY`. The derived photometric offsets are reported in Table 3, which were then validated by fitting a subset at fixed, spectroscopically-confirmed redshifts to confirm that the ratio of the template and observed population SEDs were consistent with unity in the HST and NIRCam bands. The validated photometric offsets were then adopted in determining the photometric redshifts for all sources by again refitting using `EAZY`. We compute separate photometric redshift catalogs for photometry using `CIRC1` ($r = 0.1''$) circular apertures on the filter mosaics (`PHOTOZ`, see Appendix A.11 below) and `KRON_CONV` ellipsoidal apertures on the common-PSF mosaics (`PHOTOZ_KRON`, see Appendix A.12 below). The `CIRC1`-based photometry provides high SNR, which allows for photometric breaks to be identified cleanly and improves drop-out selections. The `KRON`-based photometry provides better measures of the total

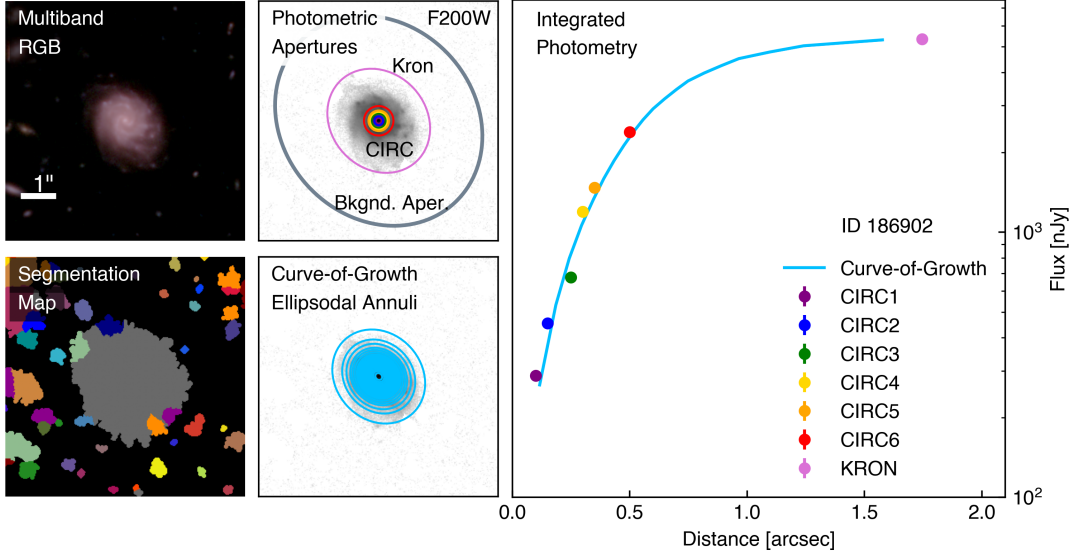


Figure 6. Overview of the photometric measurements provided in the JADES DR5 catalogs. The multi-band DR5 mosaics (upper left panel, shown as RGB) provide the pixel data for measuring the source photometry (see J26). After the detection and deblending methods in Section 3 are applied, a segmentation map for the source and the surrounding region is available (lower left panel; gray segment). The segmentation and the flux images are inputs to the source property determination methods described in Section 4, which calculate the source centroid and Kron aperture (shown as orchid ellipse overlaid on F200W image, upper middle panel). The various circular apertures allow for the CIRC photometric measures about the centroid (upper middle panel, rainbow color circles). An ellipsoidal annulus aperture at a distance of twice the Kron aperture size is used to determine the local background, and used to correct some of the photometric measures (i.e., KRON, GROWTH, and CIRC_BSUB). The curve-of-growth annuli are placed at locations containing 5% increments of the FLUX_TOT flux measured within twice the Kron aperture, and as indicated here for sources with a flat curve-of-growth the maximum aperture size A_100 where FLUX_TOT is reached can fall within even the Kron aperture. The far right panel compares the background-subtracted flux measurements for the various circular apertures (rainbow-colored points), the Kron aperture photometry (orchid point, circularized distance), and the curve-of-growth (blue line, circularized distances).

object flux and uses common-PSF images to avoid chromatic effects for extended objects, with the goal of fitting SED models with unbiased colors.

For each source, the χ^2 surface computed from the differences between the best rescaled template and the photometric data is recorded. The minimum of this curve defines the best photometric redshift z_a . Assuming a flat redshift prior, we compute the photometric redshift probability distribution as $p(z) = \exp[-\chi^2(z)/2]$ and then renormalize the distribution such that $\int p(z)dz = 1$. This computation allows us to record the probability that sources lie in excess of certain redshift thresholds or calculate the marginal percentiles on the cumulative redshift probability distributions. The shape of the $\chi^2(z)$ also enables the identification of local minima where possible low-redshift solutions for high-redshift candidate objects are permitted, and these alternative, potentially low-probability solutions are also recorded. We elaborate on which statistics are provided in the JADES DR5 catalogs in Appendices A.11 and A.12.

Figure 7 compares the photometric redshifts z_p and spectroscopic redshifts z_s for a subsample of $\approx 12,500$ JADES DR5 sources in GOODS-S and GOODS-N. The spectroscopic redshifts are taken from a compilation by D. Puskás (priv. comm.). This compilation includes sources selected from catalogs published by A. L. R. Danielson et al. (2017), T. Urrutia et al. (2019), J. Pharo et al. (2022), P. Arrabal Haro et al. (2023), R. Bacon et al. (2023), J. Chisholm et al. (2024), and DESI Collaboration et al. (2024), as well as spectroscopic determinations made from the ALMA Spectroscopic Survey in the Hubble Ultra Deep Field (ASPECS; J. González-López et al. 2019; L. A. Boogaard et al. 2020), the Observing All Phases of Stochastic Star Formation program (OASIS, JWST PID 5997; Looser et al., in prep.), the NIRSpec Wide GTO Survey (M. V. Maseda et al. 2024), JWST PID 2198 (L. Barrufet et al. 2025), JWST PID 4540 (D. J. Eisenstein et al. 2025), the JADES Transient Survey (JWST PID 6541; C. DeCoursey et al. 2025), Dark Horse (F. D'Eugenio et al. 2025b), and FRESCO (P. A. Oesch et al. 2023) referenced from the literature. These redshifts are supplemented by the JADES DR4 spectroscopic catalog (E. Curtis-Lake et al. 2025; J. Scholtz et al. 2025) and spectra from prior JADES releases (A. J. Bunker et al. 2024; F. D'Eugenio et al. 2025a). Normalized

Table 3. EAZY-derived Photometric Offsets

| Instrument | Filter | Offset |
|-------------|--------|--------|
| HST/ACS | F435W | 1.16 |
| HST/ACS | F606W | 1.07 |
| HST/ACS | F775W | 1.07 |
| HST/ACS | F814W | 1.07 |
| HST/ACS | F850LP | 0.95 |
| JWST/NIRCam | All | 1.0 |

NOTE—The photometric offsets are multiplicative factors to the flux in each filter. The same photometric offsets are applied to photometric redshift determinations for objects in both GOODS-S and GOODS-N.

histograms of the locations of $\text{F444W SNR} > 5$ sources in the z_s - z_p plane are shown for the CIRC1 (upper row) and KRON_CONV (bottom row) photometric redshift determinations for the GOODS-S (left column) and GOODS-N (right column) subfields within JADES. Overall, we find good agreement between the spectroscopic and photometric redshifts. Following the previous JADES photometric redshift performance assessment in [M. J. Rieke et al. \(2023\)](#), we define the normalized mean absolute deviation (NMAD) scatter

$$\sigma_{\text{NMAD}} = 1.48 \times \text{median} \left(\left| \frac{\delta z - \text{median}(\delta z)}{1 + z_s} \right| \right) \quad (30)$$

where $\delta z \equiv z_s - z_p$. We find $\sigma_{\text{NMAD}} = 0.028 - 0.029$ for GOODS-S and $\sigma_{\text{NMAD}} = 0.044 - 0.045$ for GOODS-N, compared with the $\sigma_{\text{NMAD}} = 0.024$ reported for a smaller subsample of JADES GOODS-S galaxies in [M. J. Rieke et al. \(2023\)](#). We note that for our EAZY fits with these templates, photometric redshift failures occur for both Balmer/4000Å breaks mimicking Lyman- α breaks and vice versa, which are apparent as spurs above and below the $z_p = z_s$ locus. In each panel, the number of catastrophic outliers decreases significantly at $z_s > 6$ where the Lyman- α break is redshifted into the NIRCam wavelength coverage. We provide a more detailed comparison of the spectroscopic and photometric redshifts for high-redshift ($z > 8$) JADES DR5 sources in Hainline et al. (submitted).

12. SUMMARY AND DATA ACCESS

In this work we have detailed the process for the generation and cataloging of the photometric source population in the JADES Data Release 5 and provided detection and deblending images, segmentation maps, aperture photometry, curve-of-growth, and photometric redshift catalogs in 35 space-based filters from James Webb Space Telescope and Hubble Space Telescope. We briefly summarize these efforts below.

- Signal-to-noise detection images were generated from a stack of long-wavelength ($\lambda > 2.5\mu\text{m}$) NIRCam mosaics, supplemented with MIRI or HST data where NIRCam coverage was unavailable (Section 3.2).
- Deblending mosaics were created from a stack of red short-wavelength ($\lambda \approx 2\mu\text{m}$) NIRCam module images, supplemented with detection image data where the desired deblending data was unavailable (Section 3.3).
- Customized detection and deblending algorithms were performed to identify and isolate faint sources in crowded, deep extragalactic fields (Section 3). The source catalogs were manually curated using an interactive web interface based on `FitsMap` ([R. Hausen & B. E. Robertson 2022](#)) (Section 3.5).
- Source properties were determined from the detection image data by performing a newly-presented method for fast Gaussian regression fits to all objects to determine source sizes and apertures for Kron photometry (Section 4).
- Custom model point-spread-functions were generated for the NIRCam images (Section 5.3) following the method of [Z. Ji et al. \(2024\)](#), or measured empirically for HST mosaics, and then used to create common-PSF mosaics (Section 6) and compute aperture corrections.

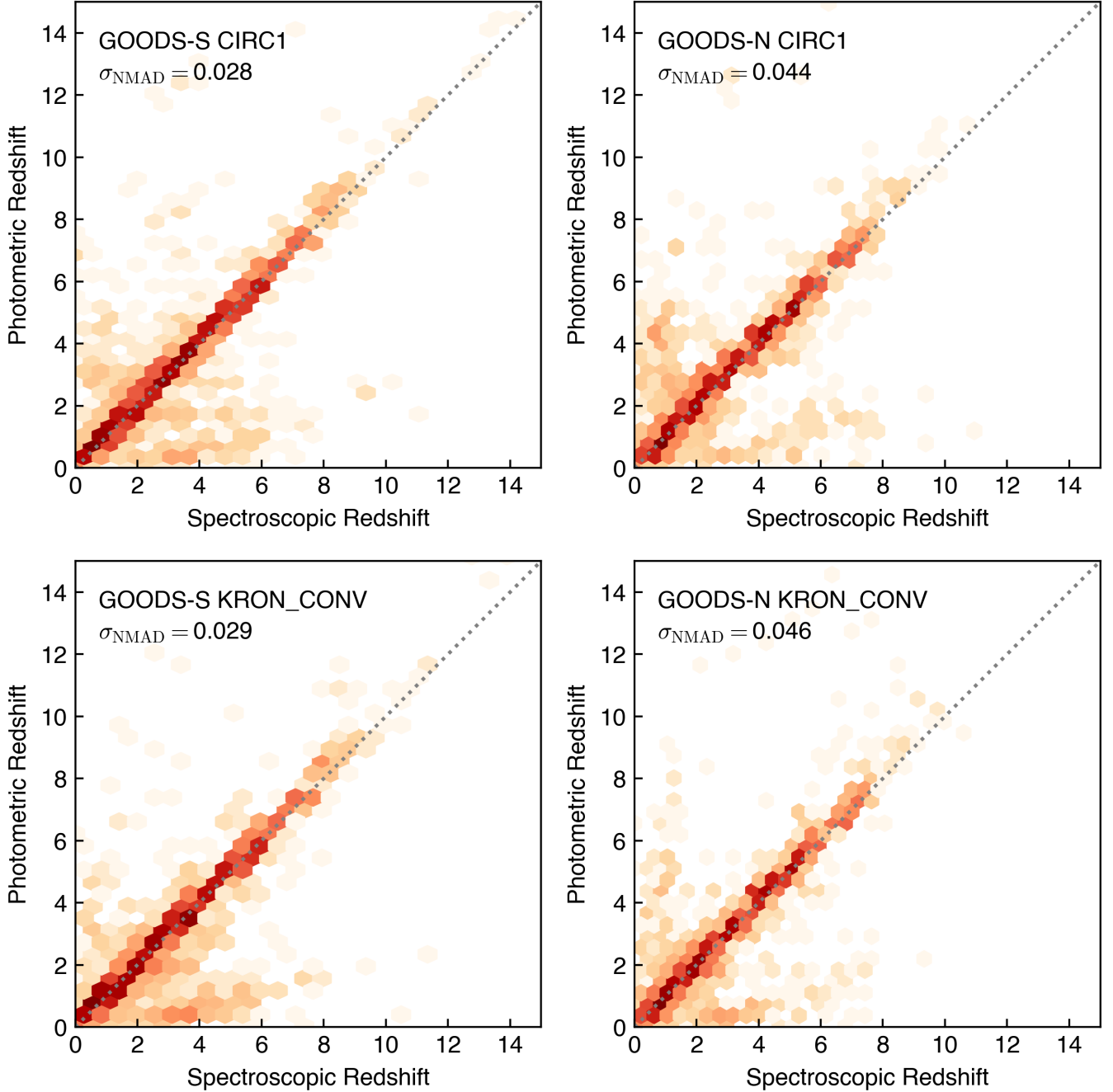


Figure 7. Comparison of photometric redshift z_p determined from the JADES DR5 catalog data using the methods described in Section 11 with spectroscopic redshift z_s for F444W SNR > 5 sources. Shown are normalized two-dimensional histograms of z_p vs. z_s for EAZY (G. B. Brammer et al. 2008) template-based photometric redshifts using CIRC1 (upper row) or KRON_CONV photometry (bottom row) for sources in GOODS-S (left column) and GOODS-N (right column). The literature references for the spectroscopic redshifts are provided in Section 11. Measures of the fractional normalized mean absolute deviation (NMAD) σ_{NMAD} in $(1+z)$ between the photometric and spectroscopic redshift are reported, which are typically 2.8-4.5%.

- Sources were annotated with data quality and context flags (Section 7) including a new hash encoding method to track the contribution of distinct JWST Programs to data on individual sources.

- Photometric uncertainty contributions from the sky background were computed using a new method that jointly fits the scaling of the RMS uncertainty in apertures of different sizes and uses the source-free inverse variance image as a template for the single-pixel uncertainty (Section 8).
- Forced photometry is performed for 35 space-based filters for \sim 500,000 sources in six circular apertures, with and without local background subtraction, and on both the intrinsic resolution and common-PSF mosaics (Section 9). Ellipsoidal aperture Kron photometry is also performed for every source on both intrinsic resolution and common-PSF mosaics (Section 9.2).
- For every source, across twenty separate ellipsoidal aperture sizes, the photometric curve-of-growth is tabulated for every filter (Section 10). These curve-of-growth catalogs allow for users to define their own total flux measurements in ellipsoidal apertures for any source in the catalog.
- Photometric redshift catalogs are generated using a template-fitting approach with the EAZY code (G. B. Brammer et al. 2008) applied separately to small ($r = 0.1''$; CIRC1) circular aperture photometry on intrinsic resolution images and Kron aperture photometry on common-PSF images.

The JADES DR5 photometric catalogs will be available along side the imaging data presented by J26 at the Mikulski Archive for Space Telescopes as a High Level Science Product via [10.17909/8tdj-8n28](https://doi.org/10.17909/8tdj-8n28). The catalogs will also be available through our interactive FitsMap (R. Hausen & B. E. Robertson 2022) website at <https://jades.idies.jhu.edu>.

ACKNOWLEDGMENTS

BER, BDJ, DJE, CC, JHM, MR, CNAW, and YZ acknowledge support from the NIRCam Science Team contract to the University of Arizona, NAS5-02105. Support for JWST programs 3215 and 5015 were provided by NASA through a grant from the Space Telescope Science Institute, which is operated by the Association of Universities for Research in Astronomy, Inc., under NASA contract NAS 5-03127. ST acknowledges support by the Royal Society Research Grant G125142. DJE is supported as a Simons Investigator. S. Alberts acknowledges support from the JWST Mid-Infrared Instrument (MIRI) Science Team Lead, grant 80NSSC18K0555, from NASA Goddard Space Flight Center to the University of Arizona. S. Arribas acknowledges grant PID2021-127718NB-I00 funded by the Spanish Ministry of Science and Innovation/State Agency of Research (MICIN/AEI/ 10.13039/501100011033). WMB gratefully acknowledges support from DARK via the DARK fellowship. This work was supported by a research grant (VIL54489) from VILLUM FONDEN. AJB & AJC acknowledge funding from the “FirstGalaxies” Advanced Grant from the European Research Council (ERC) under the European Union’s Horizon 2020 research and innovation programme (Grant agreement No. 789056). SC acknowledges support by European Union’s HE ERC Starting Grant No. 101040227 - WINGS. ECL acknowledges support of an STFC Webb Fellowship (ST/W001438/1). ALD thanks the University of Cambridge Harding Distinguished Postgraduate Scholars Programme and Technology Facilities Council (STFC) Center for Doctoral Training (CDT) in Data intensive science at the University of Cambridge (STFC grant number 2742605) for a PhD studentship. Funding for RH’s research was provided by the Johns Hopkins University, Institute for Data Intensive Engineering and Science (IDIES). JMH is supported by JWST Program 3215. RM acknowledges support by the Science and Technology Facilities Council (STFC), by the ERC through Advanced Grant 695671 “QUENCH”, and by the UKRI Frontier Research grant RISEandFALL. RM also acknowledges funding from a research professorship from the Royal Society. PGP-G acknowledges support from grant PID2022-139567NB-I00 funded by Spanish Ministerio de Ciencia e Innovación MCIN/AEI/10.13039/501100011033, FEDER, UE. JAAT acknowledges support from the Simons Foundation. HÜ acknowledges funding by the European Union (ERC APEX, 101164796). Views and opinions expressed are however those of the authors only and do not necessarily reflect those of the European Union or the European Research Council Executive Agency. Neither the European Union nor the granting authority can be held responsible for them. LW acknowledges support from the Gavin Boyle Fellowship at the Kavli Institute for Cosmology, Cambridge and from the Kavli Foundation. The research of CCW is supported by NOIRLab, which is managed by the Association of Universities for Research in Astronomy (AURA) under a cooperative agreement with the National Science Foundation.

This work is based on observations made with the NASA/ESA/CSA James Webb Space Telescope. The data were obtained from the Mikulski Archive for Space Telescopes at the Space Telescope Science Institute, which is operated

by the Association of Universities for Research in Astronomy, Inc., under NASA contract NAS 5-03127 for JWST. JADES DR5 includes NIRCam data from JWST programs 1176, 1180, 1181, 1210, 1264, 1283, 1286, 1287, 1895, 1963, 2079, 2198, 2514, 2516, 2674, 3215, 3577, 3990, 4540, 4762, 5398, 5997, 6434, 6511, and 6541. The authors acknowledge the teams of programs 1895, 1963, 2079, 2514, 3215, 3577, 3990, 6434, and 6541 for developing their observing program with a zero-exclusive-access period. The authors acknowledge use of the *lux* supercomputer at UC Santa Cruz, funded by NSF MRI grant AST 1828315. This research made use of `photutils`, an `astropy` package for detection and photometry of astronomical sources (Bradley et al. 2025).

Facilities: JWST(NIRCam and MIRI), HST(ACS and WFC3)

Software: `astropy` ([Astropy Collaboration et al. 2013, 2018, 2022](#)), `EAZY` ([G. B. Brammer et al. 2008](#)), `FitsMap` ([R. Hausen & B. E. Robertson 2022](#)), `photutils` ([L. Bradley et al. 2025](#)), `Source Extractor` ([E. Bertin & S. Arnouts 1996](#)),

APPENDIX

A. JADES DATA RELEASE 5 PHOTOMETRIC CATALOG FORMAT

This appendix details the format of the High Level Science Product versions of the JADES DR5 photometric catalogs. These catalogs are provided as collections of tables in multi-extension Flexible Image Transport System (FITS; [D. C. Wells et al. 1981](#); [W. D. Pence et al. 2010](#)) files. Section A.1 presents the `FILTERS` Header Data Unit (HDU) that describes the DR5 filter properties and the corresponding circular aperture corrections. The `FLAG` HDU presented in Section A.2 provides information on the local data quality and context around each source, proximate sources, and the JWST programs contributing data to the photometric measurements for each object. Section A.3 describes the `SIZE` HDU that contains information on the source centroids, segmentation bounding boxes, sizes, position angles, and structural properties. In Sections A.4–A.7 the HDUs containing circular aperture photometry measures are presented. The HDUs containing Kron photometry measured on the unconvolved and common PSF images are detailed in Sections A.8 and A.9, respectively. Section A.10 presents the HDU that contains all the MIRI photometry, measured in both circular and Kron apertures. The HDUs containing the photometric redshift catalogs are detailed in Sections A.11 and A.12. Owing to their data volume, the curve-of-growth catalogs (e.g., `GROWTH` and `GROWTH_CONV`) are provided as separate multi-HDU FITS files. The structural contents of these files are presented in Sections A.13 and A.14.

A.1. `FILTERS` Header Data Unit

The `FILTERS` HDU provide information on the various band passes used in the JADES DR5 photometric catalogs. Table 4 lists each field in the HDU, their units and datatype, and brief descriptions. The filters include HST ACS F435W, F606W, F775W, F814W, and F850LP filters, HST WFC3 F105W, F125W, F140W, and F160W filters, JWST NIRCam F070W, F090W, F115W, F150W, F162M, F182M, F200W, F210M, F250M, F277W, F300M, F335M, F356W, F410M, F430M, F444W, F460M, and F480M, and JWST MIRI F560W, F770W, F1000W, F1280W, F1500W, F1800W, F2100W, and F2550W. Each filter is specified in the table by its unique `BAND` name, and its pivot wavelength (`WAVE_PIVOT`), and the minimum and maximum effective wavelengths (`WAVE_MIN` and `WAVE_MAX`). The circular aperture radius (`R_CIRC0`) encircling 80% of the total PSF flux and the aperture corrections for all the circular aperture sizes for each band are also provided.

Table 4. FILTERS Header Data Unit

| Field | Units | Datatype | Description |
|------------|---------------|----------|--|
| BAND | — | str | Telescope bandpass name (e.g., F090W) |
| WAVE_PIVOT | μm | float32 | Pivot wavelength of bandpass |
| BANDWIDTH | μm | float32 | Bandwidth of bandpass |
| WAVE_MIN | μm | float32 | Minimum effective wavelength of bandpass |
| WAVE_MAX | μm | float32 | Maximum effective wavelength of bandpass |
| R_CIRCO | arcsec | float32 | Radius encircling 80% of bandpass PSF energy |
| AC_CIRC1 | — | float32 | Aperture correction applied to bandpass CIRC1 photometry |
| AC_CIRC2 | — | float32 | Aperture correction applied to bandpass CIRC2 photometry |
| AC_CIRC3 | — | float32 | Aperture correction applied to bandpass CIRC3 photometry |
| AC_CIRC4 | — | float32 | Aperture correction applied to bandpass CIRC4 photometry |
| AC_CIRC5 | — | float32 | Aperture correction applied to bandpass CIRC5 photometry |
| AC_CIRC6 | — | float32 | Aperture correction applied to bandpass CIRC6 photometry |

NOTE—The aperture corrections are applied as multiplicative factors to circular aperture flux measurements.

A.2. FLAG Header Data Unit

Table A.2 provides the details of the FLAG HDU, which provides data quality and context information for each source. The source ID, right ascension RA and declination DEC are provided for each object, and this essential information is replicated in each subsequent HDU for convenience. For each BAND the total exposure time ($\{\text{BAND}\}_{\text{TEXP}}$) and inverse variance of the sky background ($\{\text{BAND}\}_{\text{WHT}}$) at the source location is tabulated. The number of bad or missing pixels within a region defined by the source bounding box plus a surrounding 10-pixel frame in each filter is included as $\{\text{BAND}\}_{\text{FLAG}}$. The bright neighbor flag (FLAG_BN; see Section 7.3), parent segment ID (PARENT_ID; see Section 7.4), and program ID bithash (PID_HASH; see Section 7.5 and J26) are also provided for each source.

Table 5. FLAG Header Data Unit

| Field | Units | Datatype | Description |
|---------------------------------|-------------------------------|----------|---|
| ID | — | int32 | Unique source identifier |
| RA | deg | float32 | Right ascension |
| DEC | deg | float32 | Declination |
| $\{\text{BAND}\}_{\text{FLAG}}$ | pix | int32 | Number of bad or empty pixels within the region of the object's bounding box plus a 10-pixel frame |
| $\{\text{BAND}\}_{\text{TEXP}}$ | sec | float32 | Exposure time in $\{\text{BAND}\}$ at source location |
| $\{\text{BAND}\}_{\text{WHT}}$ | $(\text{MJy}/\text{sr})^{-2}$ | float32 | Estimated inverse variance of sky background at source location |
| FLAG_BN | — | int32 | Value 1 indicates neighbor $\geq 2\times$ brighter, value 2 indicates neighbor $\geq 10\times$ brighter |
| PARENT_ID | — | int32 | Unique source identifier in blended segmentation map |
| PID_HASH | — | int32 | Bithash for JWST Program IDs contributing to this object's data |

A.3. SIZE Header Data Unit

The SIZE HDU contains information on the object size, sky coordinates, image centroid, bounding box, Kron aperture properties, and detection image pixel flux distribution. Table 6 lists the contents of the SIZE HDU. Sky positions (right ascension RA and declination DEC) are provided, corresponding to the centroid pixel positions X and Y determined as described in Section 4.1. The pixel barycenter of the light distribution is also provided in the XC and YC. The pixel bounding box of each source segmentation is recorded in the BBOX_XMIN, BBOX_XMAX, BBOX_YMIN, and BBOX_YMAX fields. The semimajor (A) and semiminor (B) sizes determined from the Gaussian regression fits, their position angle THETA, and the unscaled Kron radius R_KRON_U (see Section 9.2) are provided. The full-width at half-maximum FWHM converted from the sizes A and B is reported. The Gini coefficient of the light distribution within the segmentation of each source (i.e., J. M. Lotz et al. 2004) is noted in the GINI field.

Table 6. SIZE Header Data Unit

| Field | Units | Datatype | Description |
|-----------|--------|----------|--|
| ID | — | int32 | Unique source identifier |
| RA | deg | float32 | Right ascension |
| DEC | deg | float32 | Declination |
| X | pix | float32 | Centroid x-pixel position |
| Y | pix | float32 | Centroid y-pixel position |
| XC | pix | float32 | Barycenter x-pixel position |
| YC | pix | float32 | Barycenter y-pixel position |
| BBOX_XMIN | pix | int32 | Segmentation bounding box minimum x pixel |
| BBOX_XMAX | pix | int32 | Segmentation bounding box maximum x pixel |
| BBOX_YMIN | pix | int32 | Segmentation bounding box minimum y pixel |
| BBOX_YMAX | pix | int32 | Segmentation bounding box maximum y pixel |
| A | arcsec | float32 | 2D Gaussian model standard deviation semimajor axis |
| B | arcsec | float32 | 2D Gaussian model standard deviation semiminor axis |
| THETA | deg | float32 | 2D Gaussian model position angle of semimajor axis relative to image x-axis |
| R_KRON_U | — | float32 | Unscaled Kron radius (minimum 1.4) |
| FWHM | arcsec | float32 | Circularized full width at half maximum determined from A and B |
| GINI | — | float32 | Gini coefficient computed from detection signal image within the source segmentation |

A.4. CIRC Header Data Unit

Table 7 presents the contents of the CIRC HDU of the photometric catalog. This HDU records the aperture-corrected circular aperture fluxes for each source as measured from the unconvolved image mosaics about the source centroids and without any additional background subtraction applied to the image pixel values. Aperture fluxes in seven apertures are reported, with CIRC1-CIRC6 corresponding to aperture radii of $r = [0.1'', 0.15'', 0.25'', 0.3'', 0.35'', 0.5'']$ and CIRC0 corresponding to the aperture radius for each filter that encircles 80% of the PSF flux. The fields with the `_e` suffixes indicate uncertainties measured from the uncertainty model regression (see Section 8) and those with `_ei` suffixes indicate uncertainties measured from the mosaic `ERR` image where available.

Table 7. CIRC Header Data Unit

| Field | Units | Datatype | Description |
|-----------------|-------|----------|--|
| ID | — | int32 | Unique source identifier |
| RA | deg | float32 | Right ascension |
| DEC | deg | float32 | Declination |
| {BAND}_CIRCO | nJy | float32 | Aperture-corrected flux for filter {BAND} within a circular aperture enclosing 80% of the PSF energy |
| {BAND}_CIRCO_e | nJy | float32 | Aperture-corrected flux uncertainty for filter {BAND} determined from uncertainty model regression |
| {BAND}_CIRCO_ei | nJy | float32 | Aperture-corrected flux uncertainty determined from mosaic ERR image |
| {BAND}_CIRC1 | nJy | float32 | Aperture-corrected flux for filter {BAND} within $r = 0.1''$ circular aperture |
| {BAND}_CIRC1_e | nJy | float32 | Aperture-corrected flux uncertainty for filter {BAND} determined from uncertainty model regression |
| {BAND}_CIRC1_ei | nJy | float32 | Aperture-corrected flux uncertainty determined from mosaic ERR image |
| {BAND}_CIRC2 | nJy | float32 | Aperture-corrected flux for filter {BAND} within $r = 0.15''$ circular aperture |
| {BAND}_CIRC2_e | nJy | float32 | Aperture-corrected flux uncertainty for filter {BAND} determined from uncertainty model regression. |
| {BAND}_CIRC2_ei | nJy | float32 | Aperture-corrected flux uncertainty determined from mosaic ERR image |
| {BAND}_CIRC3 | nJy | float32 | Aperture-corrected flux for filter {BAND} within $r = 0.25''$ circular aperture |
| {BAND}_CIRC3_e | nJy | float32 | Aperture-corrected flux uncertainty for filter {BAND} determined from uncertainty model regression. |
| {BAND}_CIRC3_ei | nJy | float32 | Aperture-corrected flux uncertainty determined from mosaic ERR image |
| {BAND}_CIRC4 | nJy | float32 | Aperture-corrected flux for filter {BAND} within $r = 0.3''$ circular aperture |
| {BAND}_CIRC4_e | nJy | float32 | Aperture-corrected flux uncertainty for filter {BAND} determined from uncertainty model regression |
| {BAND}_CIRC4_ei | nJy | float32 | Aperture-corrected flux uncertainty determined from mosaic ERR image |
| {BAND}_CIRC5 | nJy | float32 | Aperture-corrected flux for filter {BAND} within $r = 0.35''$ circular aperture |
| {BAND}_CIRC5_e | nJy | float32 | Aperture-corrected flux uncertainty for filter {BAND} determined from uncertainty model regression |
| {BAND}_CIRC5_ei | nJy | float32 | Aperture-corrected flux uncertainty determined from mosaic ERR image. |
| {BAND}_CIRC6 | nJy | float32 | Aperture-corrected flux for filter {BAND} within $r = 0.5''$ circular aperture. |
| {BAND}_CIRC6_e | nJy | float32 | Aperture-corrected flux uncertainty for filter {BAND} determined from uncertainty model regression |
| {BAND}_CIRC6_ei | nJy | float32 | Aperture-corrected flux uncertainty determined from mosaic ERR image |

NOTE—The {BAND} prefix in the field names indicate for which filter the measurement was performed (e.g., F090W_CIRC1 corresponds to the $r = 0.1''$ circular aperture flux for the object in the F090W filter). The fluxes reported in the CIRC HDU reflect direct measurements on the image mosaics about the source centroids with no additional background subtraction applied.

A.5. CIRC_BSUS Header Data Unit

The CIRC_BSUS HDU provides the background-subtracted, aperture-corrected circular aperture flux for each object measured from the unconvolved image mosaics. Table 8 lists the fields provided in the HDU. The definitions of these fields largely follow those in the CIRC HDU, except the local background is measured in an annulus at radii $1.5'' < r < 1.55''$ and subtracted from the circular aperture flux. The background removed from each aperture in each filter is provided in the fields with the `_bkg` suffix.

Table 8. CIRC_BSUS Header Data Unit

| Field | Units | Datatype | Description |
|------------------|-------|----------|---|
| ID | — | int32 | Unique source identifier |
| RA | deg | float32 | Right ascension |
| DEC | deg | float32 | Declination |
| {BAND}_CIRCO | nJy | float32 | Aperture-corrected, background-subtracted flux for filter {BAND} within a circular aperture enclosing 80% of the PSF energy |
| {BAND}_CIRCO_bkg | nJy | float32 | Background subtraction value for {BAND}_CIRCO |
| {BAND}_CIRCO_e | nJy | float32 | Aperture-corrected flux uncertainty for filter {BAND} determined from uncertainty model regression |
| {BAND}_CIRCO_ei | nJy | float32 | Aperture-corrected flux uncertainty determined from mosaic ERR image |
| {BAND}_CIRC1 | nJy | float32 | Aperture-corrected, background-subtracted flux for filter {BAND} within $r = 0.1''$ circular aperture |
| {BAND}_CIRC1_bkg | nJy | float32 | Background subtraction value for {BAND}_CIRC1 |
| {BAND}_CIRC1_e | nJy | float32 | Aperture-corrected flux uncertainty for filter {BAND} determined from uncertainty model regression |
| {BAND}_CIRC1_ei | nJy | float32 | Aperture-corrected flux uncertainty determined from mosaic ERR image |
| {BAND}_CIRC2 | nJy | float32 | Aperture-corrected, background-subtracted flux for filter {BAND} within $r = 0.15''$ circular aperture |
| {BAND}_CIRC2_bkg | nJy | float32 | Background subtraction value for {BAND}_CIRC2 |
| {BAND}_CIRC2_e | nJy | float32 | Aperture-corrected flux uncertainty for filter {BAND} determined from uncertainty model regression |
| {BAND}_CIRC2_ei | nJy | float32 | Aperture-corrected flux uncertainty determined from mosaic ERR image |
| {BAND}_CIRC3 | nJy | float32 | Aperture-corrected, background-subtracted flux for filter {BAND} within $r = 0.25''$ circular aperture |
| {BAND}_CIRC3_bkg | nJy | float32 | Background subtraction value for {BAND}_CIRC3 |
| {BAND}_CIRC3_e | nJy | float32 | Aperture-corrected flux uncertainty for filter {BAND} determined from uncertainty model regression |
| {BAND}_CIRC3_ei | nJy | float32 | Aperture-corrected flux uncertainty determined from mosaic ERR image |
| {BAND}_CIRC4 | nJy | float32 | Aperture-corrected, background-subtracted flux for filter {BAND} within $r = 0.3''$ circular aperture |
| {BAND}_CIRC4_bkg | nJy | float32 | Background subtraction value for {BAND}_CIRC4 |
| {BAND}_CIRC4_e | nJy | float32 | Aperture-corrected flux uncertainty for filter {BAND} determined from uncertainty model regression |
| {BAND}_CIRC4_ei | nJy | float32 | Aperture-corrected flux uncertainty determined from mosaic ERR image |
| {BAND}_CIRC5 | nJy | float32 | Aperture-corrected, background-subtracted flux for filter {BAND} within $r = 0.35''$ circular aperture |
| {BAND}_CIRC5_bkg | nJy | float32 | Background subtraction value for {BAND}_CIRC5 |
| {BAND}_CIRC5_e | nJy | float32 | Aperture-corrected flux uncertainty for filter {BAND} determined from uncertainty model regression |
| {BAND}_CIRC5_ei | nJy | float32 | Aperture-corrected flux uncertainty determined from mosaic ERR image |
| {BAND}_CIRC6 | nJy | float32 | Aperture-corrected, background-subtracted flux for filter {BAND} within $r = 0.5''$ circular aperture |
| {BAND}_CIRC6_bkg | nJy | float32 | Background subtraction value for {BAND}_CIRC6 |
| {BAND}_CIRC6_e | nJy | float32 | Aperture-corrected flux uncertainty for filter {BAND} determined from uncertainty model regression |
| {BAND}_CIRC6_ei | nJy | float32 | Aperture-corrected flux uncertainty determined from mosaic ERR image |

NOTE—The {BAND} prefix in the field names indicate for which filter the measurement was performed (e.g., F090W_CIRC1 corresponds to the $r = 0.1''$ circular aperture flux for the object in the F090W filter). The fluxes reported in the CIRC_BSUS HDU reflect measurements on the image mosaics about the source centroids, after a local background estimated from an annulus at radii $1.5'' < r < 1.55''$ is subtracted from the aperture fluxes. The subtracted background values are provided in the fields labeled with the `_bkg` suffix.

A.6. CIRC_CONV Header Data Unit

The aperture-corrected circular aperture flux and uncertainties measured from the common PSF images in each filter are provided in the CIRC_CONV HDU. Table 9 lists the fields in this HDU, which are defined the same manner as for the CIRC HDU. The aperture corrections for the common PSF images blueward of F444W are determined from the target F444W mPSF.

Table 9. CIRC_CONV Header Data Unit

| Field | Units | Datatype | Description |
|-----------------|-------|----------|---|
| ID | — | int32 | Unique source identifier |
| RA | deg | float32 | Right ascension |
| DEC | deg | float32 | Declination |
| {BAND}_CIRCO | nJy | float32 | Aperture-corrected flux for filter {BAND} common-PSF image within a circular aperture enclosing 80% of the PSF energy |
| {BAND}_CIRCO_e | nJy | float32 | Aperture-corrected flux uncertainty for filter {BAND} determined from uncertainty model regression |
| {BAND}_CIRCO_ei | nJy | float32 | Aperture-corrected flux uncertainty determined from common-PSF ERR image |
| {BAND}_CIRC1 | nJy | float32 | Aperture-corrected flux for filter {BAND} common-PSF image within $r = 0.1''$ circular aperture |
| {BAND}_CIRC1_e | nJy | float32 | Aperture-corrected flux uncertainty for filter {BAND} determined from uncertainty model regression |
| {BAND}_CIRC1_ei | nJy | float32 | Aperture-corrected flux uncertainty determined from common-PSF ERR image |
| {BAND}_CIRC2 | nJy | float32 | Aperture-corrected flux for filter {BAND} common-PSF image within $r = 0.15''$ circular aperture |
| {BAND}_CIRC2_e | nJy | float32 | Aperture-corrected flux uncertainty for filter {BAND} determined from uncertainty model regression. |
| {BAND}_CIRC2_ei | nJy | float32 | Aperture-corrected flux uncertainty determined from mosaic ERR image |
| {BAND}_CIRC3 | nJy | float32 | Aperture-corrected flux for filter {BAND} common-PSF image within $r = 0.25''$ circular aperture |
| {BAND}_CIRC3_e | nJy | float32 | Aperture-corrected flux uncertainty for filter {BAND} determined from uncertainty model regression. |
| {BAND}_CIRC3_ei | nJy | float32 | Aperture-corrected flux uncertainty determined from common-PSF ERR image |
| {BAND}_CIRC4 | nJy | float32 | Aperture-corrected flux for filter {BAND} common-PSF image within $r = 0.3''$ circular aperture |
| {BAND}_CIRC4_e | nJy | float32 | Aperture-corrected flux uncertainty for filter {BAND} determined from uncertainty model regression |
| {BAND}_CIRC4_ei | nJy | float32 | Aperture-corrected flux uncertainty determined from mosaic ERR image |
| {BAND}_CIRC5 | nJy | float32 | Aperture-corrected flux for filter {BAND} common-PSF image within $r = 0.35''$ circular aperture |
| {BAND}_CIRC5_e | nJy | float32 | Aperture-corrected flux uncertainty for filter {BAND} determined from uncertainty model regression |
| {BAND}_CIRC5_ei | nJy | float32 | Aperture-corrected flux uncertainty determined from common-PSF ERR image. |
| {BAND}_CIRC6 | nJy | float32 | Aperture-corrected flux for filter {BAND} common-PSF image within $r = 0.5''$ circular aperture. |
| {BAND}_CIRC6_e | nJy | float32 | Aperture-corrected flux uncertainty for filter {BAND} determined from uncertainty model regression |
| {BAND}_CIRC6_ei | nJy | float32 | Aperture-corrected flux uncertainty determined from common-PSF ERR image |

NOTE—The fields in the CIRC_CONV HDU are defined in the same manner as for the CIRC HDU (see Table 7, but are measured from common PSF mosaics for each filter.

A.7. CIRC_BSUS_CONV Header Data Unit

Table 10 lists the contents of the CIRC_BSUS_CONV HDU, which provides the aperture-corrected circular aperture fluxes and uncertainties measured on the common PSF images after a local background subtraction is applied. As with the values in the CIRC_CONV HDU, the background subtraction applied to the flux fields in this HDU are measured in an annulus extending over radii $1.5'' < r < 1.55''$ and the actual background corrections applied to each object in each filter are recorded in the fields with the `_bkg` suffix. The aperture corrections are computed from the target F444W mPSF.

Table 10. CIRC_BSUS_CONV Header Data Unit

| Field | Units | Datatype | Description |
|------------------|-------|----------|--|
| ID | — | int32 | Unique source identifier |
| RA | deg | float32 | Right ascension |
| DEC | deg | float32 | Declination |
| {BAND}_CIRCO | nJy | float32 | Aperture-corrected, background-subtracted flux for filter {BAND} common-PSF image within a circular aperture enclosing 80% of the PSF energy |
| {BAND}_CIRCO_bkg | nJy | float32 | Common PSF image background subtraction value for {BAND}_CIRCO |
| {BAND}_CIRCO_e | nJy | float32 | Aperture-corrected flux uncertainty for filter {BAND} determined from uncertainty model regression applied to common-PSF image |
| {BAND}_CIRCO_ei | nJy | float32 | Aperture-corrected flux uncertainty determined from common-PSF ERR image |
| {BAND}_CIRC1 | nJy | float32 | Aperture-corrected, background-subtracted flux for filter {BAND} common-PSF image within $r = 0.1''$ circular aperture |
| {BAND}_CIRC1_bkg | nJy | float32 | Common PSF image background subtraction value for {BAND}_CIRC1 |
| {BAND}_CIRC1_e | nJy | float32 | Aperture-corrected flux uncertainty for filter {BAND} determined from uncertainty model regression applied to common-PSF image |
| {BAND}_CIRC1_ei | nJy | float32 | Aperture-corrected flux uncertainty determined from common-PSF ERR image |
| {BAND}_CIRC2 | nJy | float32 | Aperture-corrected, background-subtracted flux for filter {BAND} common-PSF image within $r = 0.15''$ circular aperture |
| {BAND}_CIRC2_bkg | nJy | float32 | Common PSF image background subtraction value for {BAND}_CIRC2 |
| {BAND}_CIRC2_e | nJy | float32 | Aperture-corrected flux uncertainty for filter {BAND} determined from uncertainty model regression applied to common-PSF image |
| {BAND}_CIRC2_ei | nJy | float32 | Aperture-corrected flux uncertainty determined from common-PSF ERR image |
| {BAND}_CIRC3 | nJy | float32 | Aperture-corrected, background-subtracted flux for filter {BAND} common-PSF image within $r = 0.25''$ circular aperture |
| {BAND}_CIRC3_bkg | nJy | float32 | Common PSF image background subtraction value for {BAND}_CIRC3 |
| {BAND}_CIRC3_e | nJy | float32 | Aperture-corrected flux uncertainty for filter {BAND} determined from uncertainty model regression applied to common-PSF image |
| {BAND}_CIRC3_ei | nJy | float32 | Aperture-corrected flux uncertainty determined from common-PSF ERR image |
| {BAND}_CIRC4 | nJy | float32 | Aperture-corrected, background-subtracted flux for filter {BAND} common-PSF image within $r = 0.3''$ circular aperture |
| {BAND}_CIRC4_bkg | nJy | float32 | Common PSF image background subtraction value for {BAND}_CIRC4 |
| {BAND}_CIRC4_e | nJy | float32 | Aperture-corrected flux uncertainty for filter {BAND} determined from uncertainty model regression applied to common-PSF image |
| {BAND}_CIRC4_ei | nJy | float32 | Aperture-corrected flux uncertainty determined from common-PSF ERR image |
| {BAND}_CIRC5 | nJy | float32 | Aperture-corrected, background-subtracted flux for filter {BAND} common-PSF image within $r = 0.35''$ circular aperture |
| {BAND}_CIRC5_bkg | nJy | float32 | Common PSF image background subtraction value for {BAND}_CIRC5 |
| {BAND}_CIRC5_e | nJy | float32 | Aperture-corrected flux uncertainty for filter {BAND} determined from uncertainty model regression applied to common-PSF image |
| {BAND}_CIRC5_ei | nJy | float32 | Aperture-corrected flux uncertainty determined from common-PSF ERR image |
| {BAND}_CIRC6 | nJy | float32 | Aperture-corrected, background-subtracted flux for filter {BAND} common-PSF image within $r = 0.5''$ circular aperture |
| {BAND}_CIRC6_bkg | nJy | float32 | Common PSF image background subtraction value for {BAND}_CIRC6 |
| {BAND}_CIRC6_e | nJy | float32 | Aperture-corrected flux uncertainty for filter {BAND} determined from uncertainty model regression applied to common-PSF image |
| {BAND}_CIRC6_ei | nJy | float32 | Aperture-corrected flux uncertainty determined from common-PSF ERR image |

NOTE—The fields in this table follow the same definitions as the properties listed in Table 9 and are measured on the common PSF images, but the flux values reported here include a local background subtraction determined from an annulus extending over radii $1.5'' < r < 1.55''$. The aperture corrections in this HDU are determined from the target F444W mPSF.

A.8. KRON Header Data Unit

The KRON HDU contains information about the ellipsoidal aperture R. G. Kron (1980) photometry for each source, measured as described in Section 9.2. Table 11 lists the quantities recorded in the HDU. Object properties are provided for a Kron parameter $k = 2.5$ (_KRON suffix) and $k = 1.4$ (_KRON_S suffix). The semimajor and semiminor axes of the ellipsoidal Kron aperture are provided along with the position angle measured counter-clockwise relative to the image x -axis. The Kron flux in each filter have a local background subtraction applied, and the background (quantities with _bkg suffix) is measured in an 4-pixel-wide ellipsoidal aperture located at twice the $k = 2.5$ Kron aperture with the same axis ratio. Uncertainties measured from the regression model (_e suffix) and from the ERR mosaic (_ei suffix) are also provided.

Table 11. KRON Header Data Unit

| Field | Units | Datatype | Description |
|-------------------|--------|----------|---|
| ID | — | int32 | Unique source identifier |
| RA | deg | float32 | Right ascension |
| DEC | deg | float32 | Declination |
| A_KRON | arcsec | float32 | Semimajor axis size of aperture defined with Kron parameter $k = 2.5$ |
| B_KRON | arcsec | float32 | Semiminor axis size of aperture defined with Kron parameter $k = 2.5$ |
| THETA_KRON | deg | float32 | Position angle of Kron aperture semimajor axis relative to image x -axis, for Kron parameter $k = 2.5$ |
| A_KRON_S | arcsec | float32 | Semimajor axis size of aperture defined with Kron parameter $k = 1.4$ |
| B_KRON_S | arcsec | float32 | Semiminor axis size of aperture defined with Kron parameter $k = 1.4$ |
| THETA_KRON_S | deg | float32 | Position angle of Kron aperture semimajor axis relative to image x axis, for Kron parameter $k = 1.4$ |
| {BAND}_KRON | nJy | float32 | Aperture-corrected, background-subtracted flux for filter {BAND} within the aperture with Kron parameter $k = 2.5$ |
| {BAND}_KRON_bkg | nJy | float32 | Background subtraction value for {BAND}_KRON with Kron parameter $k = 2.5$ |
| {BAND}_KRON_e | nJy | float32 | Aperture-corrected flux uncertainty for filter {BAND} determined from uncertainty model regression using Kron parameter $k = 2.5$ |
| {BAND}_KRON_ei | nJy | float32 | Aperture-corrected flux uncertainty determined from mosaic ERR image for aperture size with Kron parameter $k = 2.5$ |
| {BAND}_KRON_S | nJy | float32 | Aperture-corrected, background-subtracted flux for filter {BAND} within the aperture with Kron parameter $k = 1.4$ |
| {BAND}_KRON_S_bkg | nJy | float32 | Background subtraction value for {BAND}_KRON with Kron parameter $k = 1.4$ |
| {BAND}_KRON_S_e | nJy | float32 | Aperture-corrected flux uncertainty for filter {BAND} determined from uncertainty model regression using Kron parameter $k = 1.4$ |
| {BAND}_KRON_S_ei | nJy | float32 | Aperture-corrected flux uncertainty determined from mosaic ERR image using Kron parameter $k = 1.4$ |

NOTE—The fields with a $_S$ suffix use a Kron parameter $k = 1.4$, while those without the suffix use $k = 2.5$. See Section 9.2 and Appendix A.8 for more details.

A.9. KRON_CONV Header Data Unit

Table 12 provides the contents of the KRON_CONV HDU that reports the ellipsoidal R. G. Kron (1980) photometry (see Section 9.2) for each object performed on the common PSF images (see Section 6). The field definitions follow those in Section A.8 and Table 11, including the Kron parameter value designations (e.g., $_S$ suffix for quantities using $k = 1.4$ and $k = 2.5$ otherwise) and background subtraction method, but the reported values have been measured on the common PSF mosaics.

Table 12. KRON_CONV Header Data Unit

| Field | Units | Datatype | Description |
|-------------------|--------|----------|---|
| ID | — | int32 | Unique source identifier |
| RA | deg | float32 | Right ascension |
| DEC | deg | float32 | Declination |
| A_KRON | arcsec | float32 | Semimajor axis size of aperture defined with Kron parameter $k = 2.5$ |
| B_KRON | arcsec | float32 | Semiminor axis size of aperture defined with Kron parameter $k = 2.5$ |
| THETA_KRON | deg | float32 | Position angle of Kron aperture semimajor axis relative to image x axis, for Kron parameter $k = 2.5$ |
| A_KRON_S | arcsec | float32 | Semimajor axis size of aperture defined with Kron parameter $k = 1.4$ |
| B_KRON_S | arcsec | float32 | Semiminor axis size of aperture defined with Kron parameter $k = 1.4$ |
| THETA_KRON_S | deg | float32 | Position angle of Kron aperture semimajor axis relative to image x axis, for Kron parameter $k = 1.4$ |
| {BAND}_KRON | nJy | float32 | Aperture-corrected, background-subtracted flux for filter {BAND} common-PSF image within the aperture with Kron parameter $k = 2.5$ |
| {BAND}_KRON_bkg | nJy | float32 | Common PSF image background subtraction value for {BAND}_KRON with Kron parameter $k = 2.5$ |
| {BAND}_KRON_e | nJy | float32 | Aperture-corrected flux uncertainty for filter {BAND} determined from uncertainty model regression applied to common-PSF image using Kron parameter $k = 2.5$ |
| {BAND}_KRON_ei | nJy | float32 | Aperture-corrected flux uncertainty determined from common-PSF ERR image using Kron parameter $k = 2.5$ |
| {BAND}_KRON_S | nJy | float32 | Aperture-corrected, background-subtracted flux for filter {BAND} common-PSF image within the aperture with Kron parameter $k = 1.4$ |
| {BAND}_KRON_S_bkg | nJy | float32 | Common PSF image background subtraction value for {BAND}_KRON with Kron parameter $k = 1.4$ |
| {BAND}_KRON_S_e | nJy | float32 | Aperture-corrected flux uncertainty for filter {BAND} determined from uncertainty model regression applied to common-PSF image using Kron parameter $k = 1.4$ |
| {BAND}_KRON_S_ei | nJy | float32 | Aperture-corrected flux uncertainty determined from common-PSF ERR image using Kron parameter $k = 1.4$ |

NOTE—The fields with a `_S` suffix use a Kron parameter $k = 1.4$, while those without the suffix use $k = 2.5$. See Section 9.2 and Appendix A.9 for more details.

A.10. MIRI Header Data Unit

The MIRI HDU contains the photometric measurements performed on the JWST/MIRI mosaic images. All these measurements are performed on unconvolved mosaics. The HDU contains fields that record circular aperture photometry with (`_BSUB` suffix) and without (no additional suffix) background subtraction applied. The ellipsoidal R. G. Kron (1980) photometry for the MIRI filters is included, using Kron parameters of $k = 1.4$ (`_S` suffix) and $k = 2.5$ (no additional suffix). The Kron-related parameters are defined as in the KRON HDU detailed above in Section A.8.

Table 13. MIRI Header Data Unit

| Field | Units | Datatype | Description |
|-------------------------|--------|----------|---|
| ID | — | int32 | Unique source identifier |
| RA | deg | float32 | Right ascension |
| DEC | deg | float32 | Declination |
| {BAND}_CIRC{X} | nJy | float32 | Aperture-corrected flux for filter {BAND} within a circular aperture CIRC{X}, with $\{X\} \in [0 - 8]$ |
| {BAND}_CIRC{X}_bkg | nJy | float32 | Background subtraction value for {BAND}_CIRC{X} |
| {BAND}_CIRC{X}_e | nJy | float32 | Aperture-corrected flux uncertainty for filter {BAND} determined from uncertainty model regression |
| {BAND}_CIRC{X}_ei | nJy | float32 | Aperture-corrected flux uncertainty determined from mosaic ERR image |
| {BAND}_CIRC{X}_BSUB | nJy | float32 | Aperture-corr., background-sub. flux for filter {BAND} within a circular aperture CIRC{X}, with $\{X\} \in [0 - 8]$ |
| {BAND}_CIRC{X}_bkg_BSUB | nJy | float32 | Background subtraction value for {BAND}_CIRC{X}_BSUB |
| {BAND}_CIRC{X}_e_BSUB | nJy | float32 | Aperture-corrected flux uncertainty for filter {BAND} determined from uncertainty model regression |
| {BAND}_CIRC{X}_ei_BSUB | nJy | float32 | Aperture-corrected flux uncertainty determined from mosaic ERR image |
| A_KRON | arcsec | float32 | Semimajor axis size of aperture defined with Kron parameter $k = 2.5$ |
| B_KRON | arcsec | float32 | Semiminor axis size of aperture defined with Kron parameter $k = 2.5$ |
| THETA_KRON | deg | float32 | Position angle of Kron aperture semimajor axis relative to image x-axis, for Kron parameter $k = 2.5$ |
| A_KRON_S | arcsec | float32 | Semimajor axis size of aperture defined with Kron parameter $k = 1.4$ |
| B_KRON_S | arcsec | float32 | Semiminor axis size of aperture defined with Kron parameter $k = 1.4$ |
| THETA_KRON_S | deg | float32 | Position angle of Kron aperture semimajor axis relative to image x axis, for Kron parameter $k = 1.4$ |
| {BAND}_KRON | nJy | float32 | Aperture-corrected, background-subtracted flux for filter {BAND} within the aperture with Kron parameter $k = 2.5$ |
| {BAND}_KRON_bkg | nJy | float32 | Background subtraction value for {BAND}_KRON with Kron parameter $k = 2.5$ |
| {BAND}_KRON_e | nJy | float32 | Aperture-corrected flux uncertainty for filter {BAND} determined from uncertainty model regression using Kron parameter $k = 2.5$ |
| {BAND}_KRON_ei | nJy | float32 | Aperture-corrected flux uncertainty determined from mosaic ERR image for aperture size with Kron parameter $k = 2.5$ |
| {BAND}_KRON_S | nJy | float32 | Aperture-corrected, background-subtracted flux for filter {BAND} within the aperture with Kron parameter $k = 1.4$ |
| {BAND}_KRON_S_bkg | nJy | float32 | Background subtraction value for {BAND}_KRON with Kron parameter $k = 1.4$ |
| {BAND}_KRON_S_e | nJy | float32 | Aperture-corrected flux uncertainty for filter {BAND} determined from uncertainty model regression using Kron parameter $k = 1.4$ |
| {BAND}_KRON_S_ei | nJy | float32 | Aperture-corrected flux uncertainty determined from mosaic ERR image using Kron parameter $k = 1.4$ |

NOTE—The circular aperture and Kron photometry parameters for this MIRI HDU follow those for the CIRC, CIRC_BSUS, and KRON HDUs. Quantities with a _BSUB suffix have background subtraction applied. The Kron photometry fields with an _S suffix use a Kron parameter $k = 1.4$, while fields without the suffix use $k = 2.5$.

A.11. PHOTOZ Header Data Unit

Table 14 details the contents of the PHOTOZ HDU that provides photometric redshifts determined from the $r = 0.1''$ radius circular aperture photometry (CIRC1) performed on the unconvolved image mosaics. In addition to the source identifier ID, photometric redshift information inferred from the EAZY (G. B. Brammer et al. 2008) analysis discussed in Section 11 is presented. This information includes the EAZY best-fit redshift z_a , the maximum likelihood redshift $textttz_ml$, the redshift z_peak at the peak of the $\exp(-\chi^2)$ surface, confidence intervals on the photometric redshift, the probability of the source lying at selected redshifts, and information on potential low-redshift solutions. The binned photometric redshift distribution for each source is also provided in the $Prob_z_bins$ array for each z_bins redshift bin.

Table 14. PHOTOZ Header Data Unit

| Field | Units | Datatype | Description |
|----------------|-------|------------|--|
| ID | — | int32 | Unique source identifier |
| z_a | — | float32 | Photometric redshift |
| z_ml | — | float32 | Maximum-likelihood photometric redshift |
| chi_a | — | float32 | χ^2 value associated with photometric redshift |
| 168 | — | float32 | Lower 68% confidence interval on photometric redshift |
| u68 | — | float32 | Upper 68% confidence interval on photometric redshift |
| 195 | — | float32 | Lower 95% confidence interval on photometric redshift |
| u95 | — | float32 | Upper 95% confidence interval on photometric redshift |
| 199 | — | float32 | Lower 99% confidence interval on photometric redshift |
| u99 | — | float32 | Upper 99% confidence interval on photometric redshift |
| nfilt | — | float32 | Number of photometric filters used to constrain SED for photometric redshift |
| z_peak | — | float32 | Value of photometric redshift at peak of $\exp -\chi^2$ |
| chi_peak | — | float32 | Value of χ^2 at peak of $\exp -\chi^2$ |
| z025 | — | float32 | Photometric redshift at marginal 2.5% cumulative probability |
| z160 | — | float32 | Photometric redshift at marginal 16.0% cumulative probability |
| z500 | — | float32 | Median of marginal photometric redshift probability distribution |
| z840 | — | float32 | Photometric redshift at marginal 84.0% cumulative probability |
| z975 | — | float32 | Photometric redshift at marginal 97.5% cumulative probability |
| Prob_gt_5 | — | float32 | Integrated probability of photometric redshift $z > 5$ |
| Prob_gt_6 | — | float32 | Integrated probability of photometric redshift $z > 6$ |
| Prob_gt_7 | — | float32 | Integrated probability of photometric redshift $z > 7$ |
| Prob_gt_8 | — | float32 | Integrated probability of photometric redshift $z > 8$ |
| Prob_gt_9 | — | float32 | Integrated probability of photometric redshift $z > 9$ |
| chisq_z_lt_7 | — | float32 | Minimum χ^2 at photometric redshift $z < 7$ |
| z_chisq_z_lt_7 | — | float32 | Photometric redshift at minimum χ^2 at photometric redshift $z < 7$ |
| chisq_z_lt_6 | — | float32 | Minimum χ^2 at photometric redshift $z < 6$ |
| z_chisq_z_lt_6 | — | float32 | Photometric redshift at minimum χ^2 at photometric redshift $z < 6$ |
| chisq_z_lt_5 | — | float32 | Minimum χ^2 at photometric redshift $z < 5$ |
| z_chisq_z_lt_5 | — | float32 | Photometric redshift at minimum χ^2 at photometric redshift $z < 5$ |
| chisq_z_lt_4 | — | float32 | Minimum χ^2 at photometric redshift $z < 4$ |
| z_chisq_z_lt_4 | — | float32 | Photometric redshift at minimum χ^2 at photometric redshift $z < 4$ |
| z_bins | — | 22×float32 | Redshift bins for photometric redshift probability distribution |
| Prob_z_bins | — | 22×float32 | Binned photometric redshift probability distribution |

NOTE—This HDU reports photometric redshift information inferred from $r = 0.1''$ radius circular aperture (CIRC1 photometry performed on the unconvolved image mosaics, as described in Section 11 and Appendix A.11.

A.12. PHOTOZ_KRON Header Data Unit

The PHOTOZ_KRON HDU reports photometric redshift information inferred from applying EAZY (G. B. Brammer et al. 2008) to the R. G. Kron (1980) ellipsoidal aperture photometry performed on common PSF images. The details of the photometric redshift measurements are discussed in Section 11. The properties in this HDU follow the same format and units of the PHOTOZ HDU described in Appendix A.11.

Table 15. PHOTOZ_KRON Header Data Unit

| Field | Units | Datatype | Description |
|----------------|-------|------------|--|
| ID | — | int32 | Unique source identifier |
| z_a | — | float32 | Photometric redshift |
| z_ml | — | float32 | Maximum-likelihood photometric redshift |
| chi_a | — | float32 | χ^2 value associated with photometric redshift |
| 168 | — | float32 | Lower 68% confidence interval on photometric redshift |
| u68 | — | float32 | Upper 68% confidence interval on photometric redshift |
| 195 | — | float32 | Lower 95% confidence interval on photometric redshift |
| u95 | — | float32 | Upper 95% confidence interval on photometric redshift |
| 199 | — | float32 | Lower 99% confidence interval on photometric redshift |
| u99 | — | float32 | Upper 99% confidence interval on photometric redshift |
| nfilt | — | float32 | Number of photometric filters used to constrain SED for photometric redshift |
| z_peak | — | float32 | Value of photometric redshift at peak of $\exp -\chi^2$ |
| chi_peak | — | float32 | Value of χ^2 at peak of $\exp -\chi^2$ |
| z025 | — | float32 | Photometric redshift at marginal 2.5% cumulative probability |
| z160 | — | float32 | Photometric redshift at marginal 16.0% cumulative probability |
| z500 | — | float32 | Median of marginal photometric redshift probability distribution |
| z840 | — | float32 | Photometric redshift at marginal 84.0% cumulative probability |
| z975 | — | float32 | Photometric redshift at marginal 97.5% cumulative probability |
| Prob_gt_5 | — | float32 | Integrated probability of photometric redshift $z > 5$ |
| Prob_gt_6 | — | float32 | Integrated probability of photometric redshift $z > 6$ |
| Prob_gt_7 | — | float32 | Integrated probability of photometric redshift $z > 7$ |
| Prob_gt_8 | — | float32 | Integrated probability of photometric redshift $z > 8$ |
| Prob_gt_9 | — | float32 | Integrated probability of photometric redshift $z > 9$ |
| chisq_z_lt_7 | — | float32 | Minimum χ^2 at photometric redshift $z < 7$ |
| z_chisq_z_lt_7 | — | float32 | Photometric redshift at minimum χ^2 at photometric redshift $z < 7$ |
| chisq_z_lt_6 | — | float32 | Minimum χ^2 at photometric redshift $z < 6$ |
| z_chisq_z_lt_6 | — | float32 | Photometric redshift at minimum χ^2 at photometric redshift $z < 6$ |
| chisq_z_lt_5 | — | float32 | Minimum χ^2 at photometric redshift $z < 5$ |
| z_chisq_z_lt_5 | — | float32 | Photometric redshift at minimum χ^2 at photometric redshift $z < 5$ |
| chisq_z_lt_4 | — | float32 | Minimum χ^2 at photometric redshift $z < 4$ |
| z_chisq_z_lt_4 | — | float32 | Photometric redshift at minimum χ^2 at photometric redshift $z < 4$ |
| z_bins | — | 22×float32 | Redshift bins for photometric redshift probability distribution |
| Prob_z_bins | — | 22×float32 | Binned photometric redshift probability distribution |

NOTE—This HDU reports photometric redshift information inferred from ellipsoidal R. G. Kron (1980) photometry performed on the common PSF image mosaics, as described in Section 11 and Appendix A.12. The common PSF mosaics are described in Section 6 and the Kron photometry method is detailed in Section 9.2.

A.13. GROWTH Catalog

The curve-of-growth measurements described in Section 10 result in a large number of fields for each object for each of the 35 mosaic images. As a result, the curve-of-growth measurements are separated into a distinct High Level Science Product catalog with separate HDUs for each BAND labeled by its filter name (e.g., F070W). Table 16 details the contents of these 35 HDUs in the GROWTH catalog, measured from the unconvolved mosaic images. Each source identifier and sky position is provided, along with the total flux within the outer aperture of the curve of growth defined by twice the Kron aperture (see Sections 9.2 and 10). The Kron aperture semimajor and semiminor axes are reported (A_KRON and B_KRON), as well as the position angle THETA measured counter clockwise from the image x -axis. The flux uncertainty determined from model regression (_e suffix) and the ERR image (_ei suffix) are provided, including a field F_SKY_e) recording the contribution of the sky noise to the total uncertainty. The curve-of-growth measurements have a local background subtraction applied, which is reported in F_TOT_bkg and measured from the annuli defined by inner and outer semimajor axes (A_IN_BKG and A_OUT_BKG, respectively) and the Kron aperture axis ratio Q. The apertures containing 5-100% of the total flux are reported as A_5 through A_100 in 5% increments.

Table 16. GROWTH {BAND} Header Data Unit

| Field | Units | Datatype | Description |
|-----------|--------|----------|---|
| ID | — | int32 | Unique source identifier |
| RA | deg | float32 | Right ascension |
| DEC | deg | float32 | Declination |
| F_TOT | nJy | float32 | Total flux within twice the Kron aperture determined from {BAND} mosaic |
| F_SKY_e | nJy | float32 | Contribution of the sky background to the F_TOT flux uncertainty, determined from the uncertainty regression model. |
| F_TOT_ei | nJy | float32 | Uncertainty estimate for F_TOT measured from the mosaic ERR HDU. |
| F_TOT_bkg | nJy | float32 | Background subtracted from the F_TOT flux. |
| A_KRON | arcsec | float32 | Source aperture semimajor axis determined with Kron parameter $k = 2.5$ |
| B_KRON | arcsec | float32 | Source aperture semiminor axis determined with Kron parameter $k = 2.5$ |
| A_IN_BKG | arcsec | float32 | Inner ellipsoidal annulus aperture semimajor axis used to determine background. |
| A_OUT_BKG | arcsec | float32 | Outer ellipsoidal annulus aperture semimajor axis used to determine background. |
| Q | — | float32 | Axis ratio of ellipsoidal annulus used to determine background. |
| THETA | deg | float32 | Position angle of apertures relative to image x axis |
| A_5 | arcsec | float32 | Semimajor axis of ellipsoidal aperture containing 5% of F_TOT |
| A_10 | arcsec | float32 | Semimajor axis of ellipsoidal aperture containing 10% of F_TOT |
| A_15 | arcsec | float32 | Semimajor axis of ellipsoidal aperture containing 15% of F_TOT |
| A_20 | arcsec | float32 | Semimajor axis of ellipsoidal aperture containing 20% of F_TOT |
| A_25 | arcsec | float32 | Semimajor axis of ellipsoidal aperture containing 25% of F_TOT |
| A_30 | arcsec | float32 | Semimajor axis of ellipsoidal aperture containing 30% of F_TOT |
| A_35 | arcsec | float32 | Semimajor axis of ellipsoidal aperture containing 35% of F_TOT |
| A_40 | arcsec | float32 | Semimajor axis of ellipsoidal aperture containing 40% of F_TOT |
| A_45 | arcsec | float32 | Semimajor axis of ellipsoidal aperture containing 45% of F_TOT |
| A_50 | arcsec | float32 | Semimajor axis of ellipsoidal aperture containing 50% of F_TOT |
| A_55 | arcsec | float32 | Semimajor axis of ellipsoidal aperture containing 55% of F_TOT |
| A_60 | arcsec | float32 | Semimajor axis of ellipsoidal aperture containing 60% of F_TOT |
| A_65 | arcsec | float32 | Semimajor axis of ellipsoidal aperture containing 65% of F_TOT |
| A_70 | arcsec | float32 | Semimajor axis of ellipsoidal aperture containing 70% of F_TOT |
| A_75 | arcsec | float32 | Semimajor axis of ellipsoidal aperture containing 75% of F_TOT |
| A_80 | arcsec | float32 | Semimajor axis of ellipsoidal aperture containing 80% of F_TOT |
| A_85 | arcsec | float32 | Semimajor axis of ellipsoidal aperture containing 85% of F_TOT |
| A_90 | arcsec | float32 | Semimajor axis of ellipsoidal aperture containing 90% of F_TOT |
| A_95 | arcsec | float32 | Semimajor axis of ellipsoidal aperture containing 95% of F_TOT |
| A_100 | arcsec | float32 | Semimajor axis of ellipsoidal aperture containing 100% of F_TOT |

NOTE—The GROWTH catalog consists of 35 HDUs, one for each filter. The above Table lists the properties of these 35 HDUs and are measured from the unconvolved image mosaics as described in Section 10 and Appendix A.13.

A.14. *GROWTH_CONV Catalog*

Owing to the large number of measurements per object and the large number of filters in the dataset, the curve-of-growth measurements on the common PSF images are provided in a standalone GROWTH_CONV catalog. In this catalog, each of the 35 filters has a corresponding HDU with contents detailed in Table 17. The properties of these GROWTH_CONV catalog HDUs are defined in the same manner as for the GROWTH catalog, as described in Section 10 and Appendix A.13 above. These properties include the semimajor axes of apertures containing 5-100% of the total flux F_TOT of the object in increments of 5% and the axis ratio of the apertures. Flux uncertainty information is also provided for each source. We note that only filters blueward of F444W are brought to a common PSF approximating the F444W PSF, while longer wavelength filters are left unconvolved.

REFERENCES

Alberts, S., Lyu, J., Shvaei, I., et al. 2024, ApJ, 976, 224, doi: [10.3847/1538-4357/ad7396](https://doi.org/10.3847/1538-4357/ad7396)

Alberts, S., Eisenstein, D. J., Bunker, A. J., et al. submitted, ApJ

Arrabal Haro, P., Dickinson, M., Finkelstein, S. L., et al. 2023, ApJL, 951, L22, doi: [10.3847/2041-8213/acdd54](https://doi.org/10.3847/2041-8213/acdd54)

Table 17. GROWTH_CONV {BAND} Header Data Unit

| Field | Units | Datatype | Description |
|-----------|--------|----------|---|
| ID | — | int32 | Unique source identifier |
| RA | deg | float32 | Right ascension |
| DEC | deg | float32 | Declination |
| F_TOT | nJy | float32 | Total flux within twice the Kron aperture determined from common-PSF mosaic in {BAND} |
| F_SKY_e | nJy | float32 | Contribution of the sky background to the F_TOT flux uncertainty, determined from the uncertainty regression model. |
| F_TOT_ei | nJy | float32 | Uncertainty estimate for F_TOT measured from the mosaic ERR HDU. |
| F_TOT_bkg | nJy | float32 | Background subtracted from the F_TOT flux. |
| A_KRON | arcsec | float32 | Source aperture semimajor axis determined with Kron parameter $k = 2.5$ |
| B_KRON | arcsec | float32 | Source aperture semiminor axis determined with Kron parameter $k = 2.5$ |
| A_IN_BKG | arcsec | float32 | Inner ellipsoidal annulus aperture semimajor axis used to determine background. |
| A_OUT_BKG | arcsec | float32 | Outer ellipsoidal annulus aperture semimajor axis used to determine background. |
| Q | — | float32 | Axis ratio of ellipsoidal annulus used to determine background. |
| THETA | deg | float32 | Position angle of apertures relative to image x axis |
| A_5 | arcsec | float32 | Semimajor axis of ellipsoidal aperture containing 5% of F_TOT |
| A_10 | arcsec | float32 | Semimajor axis of ellipsoidal aperture containing 10% of F_TOT |
| A_15 | arcsec | float32 | Semimajor axis of ellipsoidal aperture containing 15% of F_TOT |
| A_20 | arcsec | float32 | Semimajor axis of ellipsoidal aperture containing 20% of F_TOT |
| A_25 | arcsec | float32 | Semimajor axis of ellipsoidal aperture containing 25% of F_TOT |
| A_30 | arcsec | float32 | Semimajor axis of ellipsoidal aperture containing 30% of F_TOT |
| A_35 | arcsec | float32 | Semimajor axis of ellipsoidal aperture containing 35% of F_TOT |
| A_40 | arcsec | float32 | Semimajor axis of ellipsoidal aperture containing 40% of F_TOT |
| A_45 | arcsec | float32 | Semimajor axis of ellipsoidal aperture containing 45% of F_TOT |
| A_50 | arcsec | float32 | Semimajor axis of ellipsoidal aperture containing 50% of F_TOT |
| A_55 | arcsec | float32 | Semimajor axis of ellipsoidal aperture containing 55% of F_TOT |
| A_60 | arcsec | float32 | Semimajor axis of ellipsoidal aperture containing 60% of F_TOT |
| A_65 | arcsec | float32 | Semimajor axis of ellipsoidal aperture containing 65% of F_TOT |
| A_70 | arcsec | float32 | Semimajor axis of ellipsoidal aperture containing 70% of F_TOT |
| A_75 | arcsec | float32 | Semimajor axis of ellipsoidal aperture containing 75% of F_TOT |
| A_80 | arcsec | float32 | Semimajor axis of ellipsoidal aperture containing 80% of F_TOT |
| A_85 | arcsec | float32 | Semimajor axis of ellipsoidal aperture containing 85% of F_TOT |
| A_90 | arcsec | float32 | Semimajor axis of ellipsoidal aperture containing 90% of F_TOT |
| A_95 | arcsec | float32 | Semimajor axis of ellipsoidal aperture containing 95% of F_TOT |
| A_100 | arcsec | float32 | Semimajor axis of ellipsoidal aperture containing 100% of F_TOT |

NOTE—The GROWTH_CONV catalog consists of 35 HDUs, one for each filter. The above Table lists the properties of these 35 HDUs and are measured from the common PSF image mosaics as described in Sections 6 and 10 and Appendix A.14. Note that only filters blueward of F444W are brought to a common PSF approximating F444W, while longer wavelength filters are left unconvolved.

Astropy Collaboration, Robitaille, T. P., Tollerud, E. J., et al. 2013, A&A, 558, A33, doi: [10.1051/0004-6361/201322068](https://doi.org/10.1051/0004-6361/201322068)

Astropy Collaboration, Price-Whelan, A. M., Sipőcz, B. M., et al. 2018, AJ, 156, 123, doi: [10.3847/1538-3881/aabc4f](https://doi.org/10.3847/1538-3881/aabc4f)

Astropy Collaboration, Price-Whelan, A. M., Lim, P. L., et al. 2022, ApJ, 935, 167, doi: [10.3847/1538-4357/ac7c74](https://doi.org/10.3847/1538-4357/ac7c74)

Bacon, R., Brinchmann, J., Conseil, S., et al. 2023, A&A, 670, A4, doi: [10.1051/0004-6361/202244187](https://doi.org/10.1051/0004-6361/202244187)

Bagley, M. B., Pirzkal, N., Finkelstein, S. L., et al. 2024, ApJL, 965, L6, doi: [10.3847/2041-8213/ad2f31](https://doi.org/10.3847/2041-8213/ad2f31)

Barrufet, L., Oesch, P. A., Marques-Chaves, R., et al. 2025, MNRAS, 537, 3453, doi: [10.1093/mnras/staf013](https://doi.org/10.1093/mnras/staf013)

Bertin, E., & Arnouts, S. 1996, A&AS, 117, 393, doi: [10.1051/aas:1996164](https://doi.org/10.1051/aas:1996164)

Boogaard, L. A., van der Werf, P., Weiss, A., et al. 2020, ApJ, 902, 109, doi: [10.3847/1538-4357/abb82f](https://doi.org/10.3847/1538-4357/abb82f)

Bradley, L., Sipőcz, B., Robitaille, T., et al. 2025, astropy/photutils: 2.2.0, 2.2.0 Zenodo, doi: [10.5281/zenodo.14889440](https://doi.org/10.5281/zenodo.14889440)

Brammer, G. B., van Dokkum, P. G., & Coppi, P. 2008, ApJ, 686, 1503, doi: [10.1086/591786](https://doi.org/10.1086/591786)

Bunker, A. J., NIRSPEC Instrument Science Team, & JAEss Collaboration. 2020, in IAU Symposium, Vol. 352, Uncovering Early Galaxy Evolution in the ALMA and JWST Era, ed. E. da Cunha, J. Hodge, J. Afonso, L. Pentericci, & D. Sobral, 342–346, doi: [10.1017/S1743921319009463](https://doi.org/10.1017/S1743921319009463)

Bunker, A. J., Cameron, A. J., Curtis-Lake, E., et al. 2024, A&A, 690, A288, doi: [10.1051/0004-6361/202347094](https://doi.org/10.1051/0004-6361/202347094)

Burgasser, A. J., Bezanson, R., Labbe, I., et al. 2024, *ApJ*, 962, 177, doi: [10.3847/1538-4357/ad206f](https://doi.org/10.3847/1538-4357/ad206f)

Carniani, S., Hainline, K., D'Eugenio, F., et al. 2024, *Nature*, 633, 318, doi: [10.1038/s41586-024-07860-9](https://doi.org/10.1038/s41586-024-07860-9)

Carreira, C., Robertson, B. E., Danhaive, A. L., et al. submitted, *ApJ*

Casey, C. M., Kartaltepe, J. S., Drakos, N. E., et al. 2023, *ApJ*, 954, 31, doi: [10.3847/1538-4357/acc2bc](https://doi.org/10.3847/1538-4357/acc2bc)

Castellano, M., Fontana, A., Treu, T., et al. 2022, *ApJL*, 938, L15, doi: [10.3847/2041-8213/ac94d0](https://doi.org/10.3847/2041-8213/ac94d0)

Chisholm, J., Berg, D. A., Endsley, R., et al. 2024, *MNRAS*, 534, 2633, doi: [10.1093/mnras/stae2199](https://doi.org/10.1093/mnras/stae2199)

Cox, I. G., Kartaltepe, J. S., Bagley, M. B., et al. 2025, arXiv e-prints, arXiv:2510.08743, doi: [10.48550/arXiv.2510.08743](https://doi.org/10.48550/arXiv.2510.08743)

Curtis-Lake, E., Carniani, S., Cameron, A., et al. 2023, *Nature Astronomy*, 7, 622, doi: [10.1038/s41550-023-01918-w](https://doi.org/10.1038/s41550-023-01918-w)

Curtis-Lake, E., Cameron, A. J., Bunker, A. J., et al. 2025, arXiv e-prints, arXiv:2510.01033, doi: [10.48550/arXiv.2510.01033](https://doi.org/10.48550/arXiv.2510.01033)

Danielson, A. L. R., Swinbank, A. M., Smail, I., et al. 2017, *ApJ*, 840, 78, doi: [10.3847/1538-4357/aa6caf](https://doi.org/10.3847/1538-4357/aa6caf)

DeCoursey, C., Egami, E., Pierel, J. D. R., et al. 2025, *ApJ*, 979, 250, doi: [10.3847/1538-4357/ad8fab](https://doi.org/10.3847/1538-4357/ad8fab)

DESI Collaboration, Adame, A. G., Aguilar, J., et al. 2024, *AJ*, 168, 58, doi: [10.3847/1538-3881/ad3217](https://doi.org/10.3847/1538-3881/ad3217)

D'Eugenio, F., Cameron, A. J., Scholtz, J., et al. 2025a, *ApJS*, 277, 4, doi: [10.3847/1538-4365/ada148](https://doi.org/10.3847/1538-4365/ada148)

D'Eugenio, F., Nelson, E. J., Eisenstein, D. J., et al. 2025b, arXiv e-prints, arXiv:2510.11626, doi: [10.48550/arXiv.2510.11626](https://doi.org/10.48550/arXiv.2510.11626)

Dicken, D., Marín, M. G., Shivaei, I., et al. 2024, *A&A*, 689, A5, doi: [10.1051/0004-6361/202449451](https://doi.org/10.1051/0004-6361/202449451)

Donnan, C. T., McLure, R. J., Dunlop, J. S., et al. 2024, *MNRAS*, 533, 3222, doi: [10.1093/mnras/stae2037](https://doi.org/10.1093/mnras/stae2037)

Eisenstein, D. J., Willott, C., Alberts, S., et al. 2023, arXiv e-prints, arXiv:2306.02465, doi: [10.48550/arXiv.2306.02465](https://doi.org/10.48550/arXiv.2306.02465)

Eisenstein, D. J., Johnson, B. D., Robertson, B., et al. 2025, *ApJS*, 281, 50, doi: [10.3847/1538-4365/ae1137](https://doi.org/10.3847/1538-4365/ae1137)

Erb, D. K., Pettini, M., Shapley, A. E., et al. 2010, *ApJ*, 719, 1168, doi: [10.1088/0004-637X/719/2/1168](https://doi.org/10.1088/0004-637X/719/2/1168)

Finkelstein, S. L., Bagley, M. B., Arrabal Haro, P., et al. 2022, *ApJL*, 940, L55, doi: [10.3847/2041-8213/ac966e](https://doi.org/10.3847/2041-8213/ac966e)

Finkelstein, S. L., Bagley, M. B., Arrabal Haro, P., et al. 2025, *ApJL*, 983, L4, doi: [10.3847/2041-8213/adbbd3](https://doi.org/10.3847/2041-8213/adbbd3)

Gáspár, A., Rieke, G. H., Guillard, P., et al. 2021, *PASP*, 133, 014504, doi: [10.1088/1538-3873/abcd04](https://doi.org/10.1088/1538-3873/abcd04)

González-López, J., Decarli, R., Pavesi, R., et al. 2019, *ApJ*, 882, 139, doi: [10.3847/1538-4357/ab3105](https://doi.org/10.3847/1538-4357/ab3105)

Guo, H. 2011, *IEEE Signal Processing Magazine*, 28, 134, doi: [10.1109/MSP.2011.941846](https://doi.org/10.1109/MSP.2011.941846)

Hainline, K. N., Johnson, B. D., Robertson, B., et al. 2024, *ApJ*, 964, 71, doi: [10.3847/1538-4357/ad1ee4](https://doi.org/10.3847/1538-4357/ad1ee4)

Hainline, K. N., Helton, J. M., Miles, B. E., et al. 2025, arXiv e-prints, arXiv:2510.00111, doi: [10.48550/arXiv.2510.00111](https://doi.org/10.48550/arXiv.2510.00111)

Hausen, R., & Robertson, B. 2022, arXiv e-prints, arXiv:2201.04714, doi: [10.48550/arXiv.2201.04714](https://doi.org/10.48550/arXiv.2201.04714)

Hausen, R., & Robertson, B. E. 2022, *Astronomy and Computing*, 39, 100586, doi: [10.1016/j.ascom.2022.100586](https://doi.org/10.1016/j.ascom.2022.100586)

Illingworth, G., Magee, D., Bouwens, R., et al. 2016, arXiv e-prints, arXiv:1606.00841, doi: [10.48550/arXiv.1606.00841](https://doi.org/10.48550/arXiv.1606.00841)

Ji, Z., Williams, C. C., Tacchella, S., et al. 2024, *ApJ*, 974, 135, doi: [10.3847/1538-4357/ad6e7f](https://doi.org/10.3847/1538-4357/ad6e7f)

Johnson, B. D., Robertson, B. E., Eisenstein, D. J., et al. submitted, *ApJ*

Kartaltepe, J., Rafelski, M., Alavi, A., et al. 2024, *POPIES: The Public Observation Pure Parallel Infrared Emission-Line Survey*, JWST Proposal. Cycle 3, ID. #5398

Kron, R. G. 1980, *ApJS*, 43, 305, doi: [10.1086/190669](https://doi.org/10.1086/190669)

Labbé, I., Huang, J., Franx, M., et al. 2005, *ApJL*, 624, L81, doi: [10.1086/430700](https://doi.org/10.1086/430700)

Langeroodi, D., & Hjorth, J. 2023, *ApJL*, 957, L27, doi: [10.3847/2041-8213/acfeec](https://doi.org/10.3847/2041-8213/acfeec)

Libralato, M., Argyriou, I., Dicken, D., et al. 2024, *PASP*, 136, 034502, doi: [10.1088/1538-3873/ad2551](https://doi.org/10.1088/1538-3873/ad2551)

Lotz, J. M., Primack, J., & Madau, P. 2004, *AJ*, 128, 163, doi: [10.1086/421849](https://doi.org/10.1086/421849)

Madau, P. 1995, *ApJ*, 441, 18, doi: [10.1086/175332](https://doi.org/10.1086/175332)

Maseda, M. V., de Graaff, A., Franx, M., et al. 2024, *A&A*, 689, A73, doi: [10.1051/0004-6361/202449914](https://doi.org/10.1051/0004-6361/202449914)

Melchior, P., Moolekamp, F., Jerdee, M., et al. 2018, *Astronomy and Computing*, 24, 129, doi: [10.1016/j.ascom.2018.07.001](https://doi.org/10.1016/j.ascom.2018.07.001)

Merlin, E., Santini, P., Paris, D., et al. 2024, *A&A*, 691, A240, doi: [10.1051/0004-6361/202451409](https://doi.org/10.1051/0004-6361/202451409)

Morishita, T., Mason, C. A., Kreilgaard, K. C., et al. 2025, *ApJ*, 983, 152, doi: [10.3847/1538-4357/adbbdc](https://doi.org/10.3847/1538-4357/adbbdc)

Naidu, R. P., Oesch, P. A., van Dokkum, P., et al. 2022, *ApJL*, 940, L14, doi: [10.3847/2041-8213/ac9b22](https://doi.org/10.3847/2041-8213/ac9b22)

Naidu, R. P., Oesch, P. A., Brammer, G., et al. 2025, arXiv e-prints, arXiv:2505.11263, doi: [10.48550/arXiv.2505.11263](https://doi.org/10.48550/arXiv.2505.11263)

Oesch, P. A., Brammer, G., Naidu, R. P., et al. 2023, *MNRAS*, 525, 2864, doi: [10.1093/mnras/stad2411](https://doi.org/10.1093/mnras/stad2411)

Östlin, G., Pérez-González, P. G., Melinder, J., et al. 2025, *A&A*, 696, A57, doi: [10.1051/0004-6361/202451723](https://doi.org/10.1051/0004-6361/202451723)

Pence, W. D., Chiappetti, L., Page, C. G., Shaw, R. A., & Stobie, E. 2010, *A&A*, 524, A42, doi: [10.1051/0004-6361/201015362](https://doi.org/10.1051/0004-6361/201015362)

Pérez-González, P. G., Rinaldi, P., Caputi, K. I., et al. 2024, *ApJL*, 969, L10, doi: [10.3847/2041-8213/ad517b](https://doi.org/10.3847/2041-8213/ad517b)

Pérez-González, P. G., Östlin, G., Costantin, L., et al. 2025, *ApJ*, 991, 179, doi: [10.3847/1538-4357/adf8c9](https://doi.org/10.3847/1538-4357/adf8c9)

Perrin, M. D., Sivaramakrishnan, A., Lajoie, C.-P., et al. 2014, in Society of Photo-Optical Instrumentation Engineers (SPIE) Conference Series, Vol. 9143, Space Telescopes and Instrumentation 2014: Optical, Infrared, and Millimeter Wave, ed. J. M. Oschmann, Jr., M. Clampin, G. G. Fazio, & H. A. MacEwen, 91433X, doi: [10.1117/12.2056689](https://doi.org/10.1117/12.2056689)

Pharo, J., Guo, Y., Calvo, G. B., et al. 2022, *ApJS*, 261, 12, doi: [10.3847/1538-4365/ac6cdf](https://doi.org/10.3847/1538-4365/ac6cdf)

Pontoppidan, K. M., Pickering, T. E., Laidler, V. G., et al. 2016, in Society of Photo-Optical Instrumentation Engineers (SPIE) Conference Series, Vol. 9910, Observatory Operations: Strategies, Processes, and Systems VI, ed. A. B. Peck, R. L. Seaman, & C. R. Benn, 991016, doi: [10.1117/12.2231768](https://doi.org/10.1117/12.2231768)

Quadri, R., Marchesini, D., van Dokkum, P., et al. 2007, *AJ*, 134, 1103, doi: [10.1086/520330](https://doi.org/10.1086/520330)

Rauscher, B. J., Boehm, N., Cagiano, S., et al. 2014, *PASP*, 126, 739, doi: [10.1086/677681](https://doi.org/10.1086/677681)

Rieke, G. H., Alberts, S., Shvarei, I., et al. 2024, *ApJ*, 975, 83, doi: [10.3847/1538-4357/ad6cd2](https://doi.org/10.3847/1538-4357/ad6cd2)

Rieke, M. 2020, in IAU Symposium, Vol. 352, Uncovering Early Galaxy Evolution in the ALMA and JWST Era, ed. E. da Cunha, J. Hodge, J. Afonso, L. Pentericci, & D. Sobral, 337–341, doi: [10.1017/S1743921319008950](https://doi.org/10.1017/S1743921319008950)

Rieke, M. J., Robertson, B., Tacchella, S., et al. 2023, *ApJS*, 269, 16, doi: [10.3847/1538-4365/acf44d](https://doi.org/10.3847/1538-4365/acf44d)

Robertson, B., Johnson, B. D., Tacchella, S., et al. 2024, *ApJ*, 970, 31, doi: [10.3847/1538-4357/ad463d](https://doi.org/10.3847/1538-4357/ad463d)

Robertson, B. E. 2022, *ARA&A*, 60, 121, doi: [10.1146/annurev-astro-120221-044656](https://doi.org/10.1146/annurev-astro-120221-044656)

Robertson, B. E., Tacchella, S., Johnson, B. D., et al. 2023, *Nature Astronomy*, 7, 611, doi: [10.1038/s41550-023-01921-1](https://doi.org/10.1038/s41550-023-01921-1)

Scholtz, J., Carniani, S., Parlanti, E., et al. 2025, arXiv e-prints, arXiv:2510.01034, doi: [10.48550/arXiv.2510.01034](https://doi.org/10.48550/arXiv.2510.01034)

Sérsic, J. L. 1963, Boletin de la Asociacion Argentina de Astronomia La Plata Argentina, 6, 41

Sérsic, J. L. 1968, Atlas de Galaxias Australes

Shuntov, M., Ilbert, O., Lagos, C. d. P., et al. 2025a, arXiv e-prints, arXiv:2511.05259, doi: [10.48550/arXiv.2511.05259](https://doi.org/10.48550/arXiv.2511.05259)

Shuntov, M., Akins, H. B., Paquereau, L., et al. 2025b, *A&A*, 704, A339, doi: [10.1051/0004-6361/202555799](https://doi.org/10.1051/0004-6361/202555799)

Skelton, R. E., Whitaker, K. E., Momcheva, I. G., et al. 2014, *ApJS*, 214, 24, doi: [10.1088/0067-0049/214/2/24](https://doi.org/10.1088/0067-0049/214/2/24)

Sun, F., Fudamoto, Y., Lin, X., et al. 2025, arXiv e-prints, arXiv:2503.15587, doi: [10.48550/arXiv.2503.15587](https://doi.org/10.48550/arXiv.2503.15587)

Treu, T., Roberts-Borsani, G., Bradac, M., et al. 2022, *ApJ*, 935, 110, doi: [10.3847/1538-4357/ac8158](https://doi.org/10.3847/1538-4357/ac8158)

Urrutia, T., Wisotzki, L., Kerutt, J., et al. 2019, *A&A*, 624, A141, doi: [10.1051/0004-6361/201834656](https://doi.org/10.1051/0004-6361/201834656)

Weibel, A., Oesch, P. A., Barrufet, L., et al. 2024, *MNRAS*, 533, 1808, doi: [10.1093/mnras/stae1891](https://doi.org/10.1093/mnras/stae1891)

Weibel, A., Jespersen, C. K., Oesch, P. A., et al. 2025, arXiv e-prints, arXiv:2512.14212, doi: [10.48550/arXiv.2512.14212](https://doi.org/10.48550/arXiv.2512.14212)

Wells, D. C., Greisen, E. W., & Harten, R. H. 1981, *A&AS*, 44, 363

Whitaker, K. E., Labb  , I., van Dokkum, P. G., et al. 2011, *ApJ*, 735, 86, doi: [10.1088/0004-637X/735/2/86](https://doi.org/10.1088/0004-637X/735/2/86)

Whitaker, K. E., Ashas, M., Illingworth, G., et al. 2019, *ApJS*, 244, 16, doi: [10.3847/1538-4365/ab3853](https://doi.org/10.3847/1538-4365/ab3853)

Williams, C. C., Curtis-Lake, E., Hainline, K. N., et al. 2018, *ApJS*, 236, 33, doi: [10.3847/1538-4365/aabcbb](https://doi.org/10.3847/1538-4365/aabcbb)

Williams, C. C., Tacchella, S., Maseda, M. V., et al. 2023, *ApJS*, 268, 64, doi: [10.3847/1538-4365/acf130](https://doi.org/10.3847/1538-4365/acf130)

Williams, C. C., Oesch, P. A., Weibel, A., et al. 2025, *ApJ*, 979, 140, doi: [10.3847/1538-4357/ad97bc](https://doi.org/10.3847/1538-4357/ad97bc)

Windhorst, R. A., Cohen, S. H., Jansen, R. A., et al. 2023, *AJ*, 165, 13, doi: [10.3847/1538-3881/aca163](https://doi.org/10.3847/1538-3881/aca163)